



1 **Evolution of Cloud Droplet Temperature and Lifetime in**
2 **Spatiotemporally Varying Subsaturated Environments with**
3 **Implications for Ice Nucleation at Cloud Edges**
4

5 Puja Roy^{1,2}, Robert M. Rauber², Larry Di Girolamo²
6

7 ¹Research Applications Laboratory, NSF National Center for Atmospheric Research

8 ²Department of Climate, Meteorology & Atmospheric Sciences, University of Illinois Urbana-Champaign

9 *Correspondence to:* Puja Roy (pujaroy@ucar.edu)
10

11 **Abstract.** Ice formation mechanisms in generating cells near stratiform cloud-tops, where mixing and entrainment
12 occurs in the presence of supercooled water droplets, remain poorly understood. Supercooled cloud droplet
13 temperature and lifetime may impact heterogeneous ice nucleation through contact and immersion freezing; however,
14 modeling studies normally assume droplet temperature to be spatially uniform and equal to the ambient temperature.
15 Here, we present a first-of-its-kind quantitative investigation of the temperature and lifetime of evaporating droplets,
16 considering internal thermal gradients within the droplet as well as thermal and vapor density gradients in the
17 surrounding air. Our approach employs solving the Navier-Stokes and continuity equations, coupled with heat and
18 vapor transport, using an advanced numerical model. For typical ranges of cloud droplet sizes and environmental
19 conditions, the droplet internal thermal gradients dissipate quickly (≤ 0.3 s) when droplets are introduced to new
20 subsaturated environments. However, the magnitude of droplet cooling is much greater than estimated from past
21 studies of droplet evaporation, especially for drier environments. For example, for an environment with pressure of
22 500 hPa, and ambient temperature far from the droplet of -5°C , the droplet temperature reduction can be as high as
23 24, 11, and 5°C for initial ambient relative humidities of 10%, 40%, and 70% respectively. Droplet lifetimes are found
24 to be tens of seconds longer compared to previous estimates due to weaker evaporation rates because of lower droplet
25 surface temperatures. Using these new end-of-lifetime droplet temperatures, the enhancement in activation of ice-
26 nucleating particles predicted by current ice nucleation parameterization schemes is discussed.

27

28



29 1 Introduction

30
31 Ice formation often occurs near cloud tops of stratiform clouds where ice-generating cells are frequently found in a
32 variety of cold, cloudy environments (Plummer et al., 2014; Ramelli et al., 2021). These cells play a crucial role in
33 primary ice nucleation and growth (Tessendorf et al., 2015). Evidence of mixing and entrainment and the presence of
34 supercooled liquid water within and between the highly turbulent cells has been observed (Plummer et al., 2014; Wang
35 et al., 2020; Zaremba et al., 2024). Within regions of entrainment and mixing at cloud boundaries, cloud droplets are
36 exposed to subsaturated environments and undergo evaporation that leads to droplet temperatures that could be several
37 degrees lower than that of the ambient environment (Kinzer and Gunn, 1951; Watts, 1971; Roy et al., 2023). However,
38 in modeling cloud microphysical processes, the difference in temperature between the cloud droplets and their
39 environment is generally assumed to be negligible (Pruppacher and Klett, 1997), i.e., the droplets' temperatures are
40 approximated to be the same as that of their ambient environment. This assumption is reasonable for cloud droplets
41 inside the cloud but breaks down within entrainment and mixing zones at cloud boundaries and may lead to
42 uncertainties in the numerical simulations of microphysical processes. Cloud droplet temperatures affect the calculated
43 droplet diffusional growth or evaporation rates (Roach 1976; Srivastava and Coen 1992; Marquis and Harrington
44 2005; Roy et al., 2023), and droplet lifetimes (Roy et al., 2023), radiative effects via temperature-dependent refractive
45 indices (Rowe et al. 2020), and ice formation via pathways that require supercooled liquid water droplets, such as
46 contact nucleation (Young, 1974), immersion freezing (Szakáll et al., 2021), and homogeneous nucleation
47 (Khvorostyanov and Sassen, 1998; Khain and Pinsky, 2018). These uncertainties can propagate into microphysical
48 parameterization schemes, leading to possible inadequate representation of mixed-phase cloud properties across
49 various scales (e.g., Large Eddy Simulations (LES), Cloud Resolving Models (CRM), Climate Models), impacting
50 predictions of precipitation or climate change.

51
52 Several studies have highlighted the special importance of the air-water interface of the water droplet during ice
53 nucleation. Many experimental and theoretical studies have suggested that ice initiation occurs at the droplet surface
54 (Tabazadeh et al., 2002a; Tabazadeh et al., 2002b; Djikaev et al., 2002; Satoh et al. 2002; Shaw et al., 2005) and the
55 interface thermodynamically favors the contact mode over the immersion freezing mode (Djikaev and Ruckenstein,
56 2008). Based on their laboratory observations, Tabazadeh et al., (2002a) suggested that homogeneous nucleation of
57 nitric acid dihydrate (NAD) and nitric acid trihydrate (NAT) particles within aqueous nitric acid droplets primarily
58 occurs at the droplet surface. This leads to the hypothesis that phase transformations in atmospheric aerosols may
59 predominantly be surface-based (Tabazadeh et al., 2002b), challenging the traditional theory of homogeneous
60 crystallization where freezing begins inside the volume of the droplet (Volmer, 1939). Satoh et al. (2002) studied
61 cooling and freezing in water droplets due to evaporation in an evacuated chamber and found that droplets rapidly
62 froze with significant supercooling, with the freezing initiated from the droplet surface. Studies employing molecular
63 dynamics simulations (Chushak et al., 1999, 2000) and thermodynamic calculations (Djikaev et al., 2002) additionally
64 corroborate that a crystalline nucleus preferentially forms at the droplet surface rather than within the bulk droplet
65 volume. Laboratory observations from Shaw et al., (2005) reveal that freezing temperatures are 4-5 K higher when an



66 ice-forming nucleus is closer to the surface of a supercooled water droplet compared to when it's immersed within the
67 droplet. They found that the nucleation rate at the water surface is significantly higher (by a factor of 10^{10}) than in the
68 bulk droplet, indicating that the free energy required for critical ice germ formation decreases when near the air-water
69 interface, and the jump frequency of molecules from the liquid to the solid phase may be significantly enhanced at the
70 interface. Lü et al., (2005) conducted ice nucleation experiments with acoustically levitated supercooled water droplets
71 and found that statistical analyses of nucleation rates indicate ice nucleation predominantly initiates in the vicinity of
72 the droplet surface. Therefore, given the importance of the droplet surface in ice nucleation and since evaporation is a
73 surface phenomenon, in the quest to better understand the physical mechanisms responsible for primary ice nucleation,
74 it is important to accurately investigate the thermal evolution of the evaporating droplet surface as well as the internal
75 thermal gradients within the supercooled droplet, as ice nucleation is highly temperature dependent.

76
77 Few studies in the cloud microphysics literature have carried out explicit numerical estimations and evolutions of
78 supercooled, evaporating cloud droplet temperatures and lifetimes for a wide range of environmental conditions. Roy
79 et al., (2023) provides a comprehensive review of past theoretical, numerical, or experimental studies of droplet
80 evaporation. Most of these studies examined the evaporation of raindrops for above zero temperatures (Kinzer and
81 Gunn, 1951; Watts 1971; Watts and Farhi, 1975), either assuming steady-state expressions (Beard and Pruppacher,
82 1971) or simplifying assumptions of linear dependence of saturation vapor density on temperature (Kinzer and Gunn,
83 1951; Watts 1971; Watts and Farhi, 1975). Srivastava and Coen (1992) assumed the heat storage term in the droplet
84 heat budget to be negligible, and investigated the evaporation of isolated, stationary hydrometeors by iteratively
85 solving the steady-state solutions, using saturation vapor pressure relations from Wexler (1976) to calculate the
86 saturation vapor density. Roy et al., (2023), by including the heat storage term and solving for time-dependent heat
87 and mass transfer between single, stationary cloud droplets evaporating in infinitely large, prescribed ambient
88 environments, demonstrated that the temperatures of the cloud droplets (initial radii between 30-50 μm) reach steady-
89 state quite quickly (within <0.5 s). They considered a wide range of environmental conditions and found that
90 evaporating droplet temperatures can typically be 1-5 K colder than that of the environment, with values as low as
91 ~ 10 K for low relative humidity, and low-pressure conditions near 0°C environments. Their steady-state droplet
92 temperatures agreed well with those of Srivastava and Coen (1992). They showed that the droplet temperature during
93 evaporation can be approximated by the thermodynamic wet-bulb temperature of the ambient environment. For most
94 subsaturated conditions, radiative cooling in cloud-top environments was found to play a negligible role in altering
95 evaporating droplet temperatures, except for larger droplets in environments close to saturation.

96
97 However, two main issues have not yet been accounted for in the aforementioned studies. Firstly, water droplets were
98 considered to have a uniform bulk droplet temperature, based on the assumption of infinite thermal heat conductivity
99 of water, thus ignoring the added complexity of simulating the internal thermal gradients within the droplet. (Kinzer
100 and Gunn, 1951; Watts, 1971; Srivastava and Coen, 1992, Roy et al., 2023). As several studies suggest that the droplet
101 surface plays a special role in nucleating ice and evaporation being a surface phenomenon, accurate modeling of the
102 evolution of droplet surface temperature and internal thermal gradients within the droplet volume is required to



103 correctly predict the ice nucleation rates. Secondly, to date, none of these studies considered the spatiotemporally
104 evolving effects of thermal and moisture feedback between the droplet and its immediate environment. The rationale
105 for justifying the usage of constant ambient conditions far away from the droplet was mostly based on studies where
106 ambient conditions were defined by prescribed temperature and moisture fields far away from a droplet (Sedunov,
107 1974; Eq. 7.7 of Rogers and Yau, 1989; Srivastava and Coen, 1992). A correction to the ambient conditions at a radius
108 similar to the mean distance between droplets (~ 1 mm) was shown to lead to minimal modifications for typical cloud
109 conditions (Fukuta, 1992). Thus, this assumption holds for droplets distributed homogeneously in space. Concerning
110 numerically simulating the growth and decay of a droplet population, Grabowski and Yang (2013) stated: “Cloud
111 droplets grow or evaporate because of the presence of moisture and temperature gradients in their immediate vicinity,
112 and these gradients are responsible for the molecular transport of moisture and energy between the droplet and its
113 immediate environment. One may argue that these gradients need to be resolved to represent the growth accurately.
114 Elementary considerations demonstrate that the moisture and temperature gradients in the droplet vicinity are
115 established rapidly [i.e., with a characteristic timescale of milliseconds or smaller (e.g., Vaillancourt et al. 2001, and
116 references therein)]; thus, the steady-state droplet growth equation is accurate enough. More importantly, the volume
117 affected by these gradients has a radius of approximately 10 to 20 droplet radii.... One can simply neglect molecular
118 transport processes in the immediate droplet vicinity and simulate droplet growth using the classical approach, that is,
119 by applying the supersaturation predicted by the mean (over the volume occupied by the droplet) temperature and
120 moisture fields...(see Vaillancourt et al. 2001, appendix).”

121

122 Here, we quantitatively revisit these arguments within the context of an evaporating supercooled cloud droplet. We
123 use high-resolution modeling to resolve the spatiotemporally evolving thermal and vapor density gradients in the
124 vicinity of the droplet as well as include internal heat transfer within the droplet, relaxing the assumption of infinite
125 thermal heat conductivity of water. Using an advanced numerical model, our framework employs the finite-element
126 method to solve the Navier-Stokes and continuity equations, coupled with heat and vapor diffusion, with appropriate
127 boundary conditions. The results from this study extend the findings from Roy et al. (2023) that an evaporating droplet
128 can exist at a temperature lower than that of the ambient environment, and that the temperature deviation increases
129 from the steady-state value under certain environmental conditions. This may lead to significant enhancement in ice
130 nucleation by increasing the predicted number concentrations of activated ice-nucleating particles (INPs) either
131 immersed within or externally contacting the supercooled droplet. The current study advances the numerical approach
132 presented in Roy et al. (2023) by including the impact of internal heat gradients within the droplet and spatiotemporally
133 varying heat and mass transfer between the droplet and its immediate environment. We also provide droplet lifetime
134 comparisons with estimates from Roy et al. (2023) and pure diffusion-limited evaporation calculations. The
135 implications of the evaporating supercooled cloud droplet temperatures and lifetimes on ice nucleation at cloud
136 boundaries are discussed.

137



138 2 Numerical Methodology

139 2.2 Description of COMSOL

140

141 The simulation of the spatiotemporally varying droplet temperature and radius of an evaporating cloud droplet
142 embedded in a gaseous domain is difficult to solve analytically because of the moving and shrinking boundary at the
143 surface of the evaporating droplet. These kinds of moving boundary problems are also known as Stefan problems. To
144 model this process, we have used an advanced numerical solver, COMSOL (Version 6.0), which employs a finite
145 element method to solve partial differential equations (PDEs). The Navier-Stokes and Fick's second law of diffusion
146 equation, which follows from the continuity equation, along with appropriate boundary conditions (see Sec. 3) are
147 solved to conserve mass and momentum in the whole system. The PDEs are discretized and solved along non-uniform
148 moving mesh nodes using the Arbitrary Lagrangian-Eulerian technique (Yang et al., 2014) to accurately track the
149 moving air-water interface at the droplet surface.

150

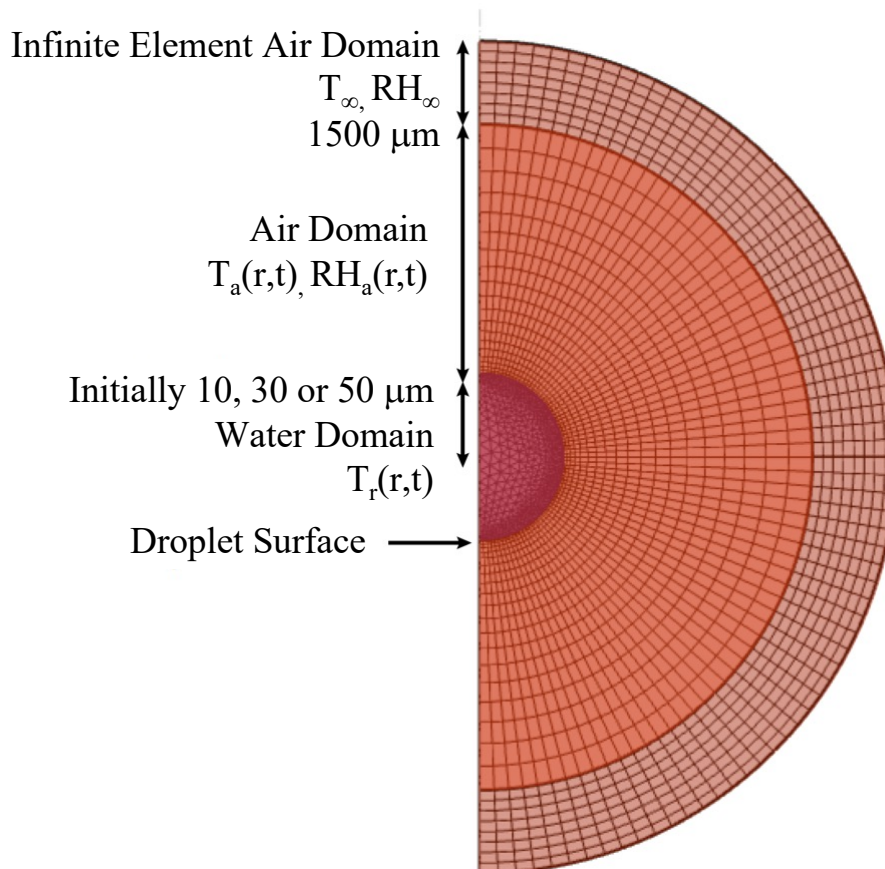
151 The COMSOL multiphysics software uses cylindrical coordinates (r, ϕ, z) to solve 2D axisymmetric geometries (z -
152 *axis* is the axis of symmetry), where r represents the radial distance from the longitudinal axis, ϕ is the azimuthal
153 angle (in the interval from $-\pi$ to π), and z is the distance from the origin along the longitudinal axis (COMSOL
154 2023a). For this modeling scenario, the geometry consists of a 2D axisymmetric domain with the center of the cloud
155 droplet at the origin (defined at $r = 0, z = 0$) with ambient air surrounding the droplet (Fig. 1). The physics interfaces
156 take care of the differential operators while solving the equations arising from the conservation laws. The following
157 physics interfaces in COMSOL were used to simulate droplet evaporation: (1) *Two-Phase Laminar Fluid Flow*, which
158 includes a moving mesh to track the shrinking water-air interface of the evaporating water droplet and fluid-fluid
159 interface that incorporates evaporative mass flux; (2) *Transport of Diluted Species* to track water vapor diffusion
160 through the air domain and predict the evaporation rate at the droplet surface; and (3) *Heat Transfer in Fluids* which
161 accounts for the non-isothermal flow within the computational domain, temperature-dependent saturation vapor
162 density at the droplet interface, and a boundary heat source to account for the latent heat of evaporation. The
163 computational domain also includes an infinite element air domain (COMSOL 2023b) to specify and maintain
164 boundary conditions far away from the droplet. The physics modules are coupled through non-isothermal flow
165 between heat transfer and fluid flow, and mass transport at the fluid-fluid interface between fluid flow and species
166 transport.

167

168 The non-uniform moving mesh, created by breaking down the computational domain into numerous fine elements of
169 variable sizes, uses the Arbitrary Lagrangian-Eulerian technique (Yang et al., 2014) to accurately track the moving
170 air-water interface at the droplet surface. In this study, we have used triangular mesh elements (COMSOL 2023c)
171 within the droplet and quadrilateral mesh elements (COMSOL 2023d) for the rest of the domain as shown in Fig. 1.
172 Finally, to simulate the water droplet evaporating in ambient air system, with appropriate initial and boundary
173 conditions, the discretized PDEs are then numerically solved along each of the mesh nodes with adaptive time steps



174 (≤ 0.01 s) to maintain numerical stability and obtain the solution (the temporal evolution of droplet temperature and
175 radius) for a range of conditions.
176



177

178

179 **Figure 1: Computational domain (not to scale) including the evaporating droplet, embedded in the air domain.**

180

181 **2.2 Justification for choice of environmental parameters in the simulations**

182

183 Probing the evolution of the droplet and its immediate environment under a wide swath of conditions was
184 computationally too expensive, thus, certain choices regarding the parameter selection were made. The assumption
185 behind the computational set-up is that the supercooled droplet is suddenly introduced to a subsaturated environment
186 with ambient temperature, $T_\infty = 273.15$ K, 268.15 K, or 263.15 K, as might happen when the droplets are near cloud
187 boundaries such as those occurring in cloud-top generating cells. These temperatures are the ones where activation of
188 INPs is thought to be least effective. Calculations presented in Sec. 4 consider three different environments having



189 ambient relative humidity, $RH_\infty = 10, 40, \text{ and } 70\%$, and two different ambient pressures, $P = 500, \text{ and } 850 \text{ hPa}$, and
190 initial cloud droplet radii, r_0 , of $10\text{-}50 \mu\text{m}$. The pressure levels were chosen based on the occurrence of 273.15 K ,
191 268.15 K , and 263.15 K in standard atmospheric profiles for tropical latitudes and middle latitudes under warm and
192 cool season conditions (Standard Atmosphere, 2021). Overall, 90 numerical experiments were performed using
193 various combinations of initial RH_∞ , T_∞ , P , and r_0 to obtain a better understanding of the relationships between the
194 evolution of droplet temperatures and radii, and environmental variables. Of these, the results of 54 experiments are
195 reported in detail herein. The results of these experiments are later summarized in Figs. 4-14 and Tables 1-2. The
196 specific combinations of environmental parameters and initial droplet radii used in this study were also selected to
197 enable easy comparison with results from a previous study of droplet evaporation (Roy et al., 2023). Also, to be noted,
198 the effect of radiation in this study was neglected based on the Roy et al. (2023), which demonstrated the negligible
199 role played by radiation in modifying evaporating droplet temperatures under most subsaturated conditions ($RH <$
200 80%).

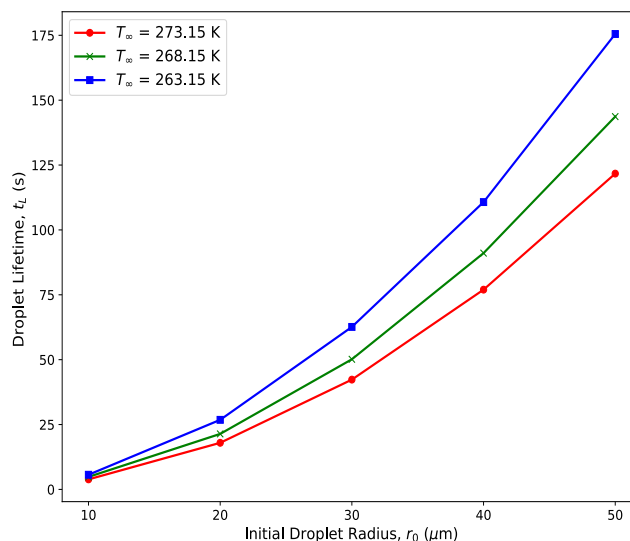
201

202 **2.3 Justification for choice of droplet lifetime cut-off**

203

204 For each experiment, the computational time rose exponentially to maintain numerical stability as the droplet radius
205 decreased during evaporation and the grid sizes needed to be smaller. To avoid exceptionally long computation time,
206 the cut-off radius for the simulations was set to be when the volume of the droplets decreased by 99.5% to reach 0.5%
207 of the initial droplet volume. For $r_0 = 10, 20, 30, 40, 50 \mu\text{m}$, the cutoff radii of the droplets are $1.71, 3.42, 5.13, 6.84,$
208 and $8.55 \mu\text{m}$, respectively. Note that due to the Raoult effect, for a solution droplet with a mass of dissolved and
209 ionized $\text{NaCl} = 10^{-13} \text{ g}$, the reduction in the evaporation rate (dr/dt) from that of a pure water droplet is about 1% for
210 a $1 \mu\text{m}$ radius droplet and 4% for a $0.7 \mu\text{m}$ droplet. As all cut-off radii considered here are $> 1 \mu\text{m}$, the solute effect
211 can be neglected. From the Kelvin equation, the equilibrium vapor pressure over a curved surface of pure water
212 approaches the value of equilibrium vapor pressure over a flat surface of pure water for a radius $> 0.01 \mu\text{m}$. Thus,
213 curvature effects were also neglected. For simplicity, we will refer to the cutoff time as the *droplet lifetime*, although
214 the droplets will survive for a longer time before complete evaporation. The droplet lifetime increases with the initial
215 droplet radius, higher atmospheric pressure, and higher RH_∞ (Fig. 2).

216



217
218 **Figure 2: Droplet lifetimes, t_L in seconds, for droplets with varying initial droplet radii, $r_0 = 10, 20, 30, 40$ and $50 \mu\text{m}$,**
219 **evaporating in an initial ambient environment with three different ambient temperatures, $T_\infty = 273.15$ (0°C), 268.15 (-5°C)**
220 **and 263.15 (-10°C) K, with relative humidity, $RH_\infty = 70\%$, with pressure, $P = 850$ hPa.**

221
222 **2.4 Sensitivity to domain size**

223
224 It was important to ensure that the spatiotemporally varying thermal and vapor density gradients in the ambient air in
225 the vicinity of the evaporating droplet don't interfere with the constant ambient conditions (RH_∞ and T_∞) at the external
226 boundary of the computational domain. Sensitivity tests with different air domain sizes of 10, 30, and 50 times the
227 initial droplet radius were carried out to determine the droplet temperature and radial dependence on domain size. It
228 was found that the evolution of droplet temperature and radius was not sensitive to domain sizes larger than 10 times
229 the droplet radius considered. Based on the sensitivity analysis, the maximum size of the computational domain for
230 all experiments was fixed at $1500 \mu\text{m}$, 30 times the largest droplet considered.

231
232 **3 Theory**

233 **3.1 Assumptions**

234
235 The framework of the numerical model assumes that an isolated, stationary, spherical, pure water droplet is suspended
236 within a 2D axisymmetric ambient air domain with constant ambient temperature ($\leq 0^\circ\text{C}$) and relative humidity
237 ($< 100\%$) at a sufficiently far distance away from the droplet that the droplet evaporation does not influence the far
238 environment. The water droplet and air are considered to be Newtonian fluids, with the assumption that no internal
239 circulation occurs within the droplet and that there is no ventilation, no radiative heat transfer, and negligible buoyancy
240 effects due to gravity. This computational approach is an advanced form of the one described in Roy et al., (2023),



241 but also includes the effect of internal droplet heat transfer and spatiotemporal gradients in temperature and vapor
242 density between the droplet and the environment (see discussion in Sec. 5).

243

244 3.2 Governing Equations

245

246 Based on the above assumptions, the following are the equations governing the system during droplet evaporation in
247 the ambient air.

248

249 (1) Fluid flow: The *Laminar Flow* interface models the weakly compressible form of the Navier-Stokes equation,
250 along with the continuity equation in the water and air domains,

251

$$252 \quad \rho \frac{\partial \mathbf{u}}{\partial t} + \rho(\mathbf{u} \cdot \nabla) \mathbf{u} = \nabla \cdot [-p\mathbf{I} + \boldsymbol{\tau}] + \mathbf{F}$$

253

$$\boldsymbol{\tau} = \mu(\nabla \mathbf{u} + (\nabla \mathbf{u})^T) - \frac{2}{3}\mu(\nabla \cdot \mathbf{u})\mathbf{I}$$

254

$$\frac{\partial \rho}{\partial t} + \nabla \cdot (\rho \mathbf{u}) = 0$$

255

256 where t is time, ρ is the fluid density (kg/m^3), \mathbf{u} is the fluid velocity vector (m/s), p is pressure (Pa), \mathbf{I} is the identity
257 tensor, $\boldsymbol{\tau}$ is the viscous stress tensor (Pa), μ is the fluid dynamic viscosity, \mathbf{F} is the external volume force vector (N/m^3),
258 which is assumed to be negligible here.

259

260

261 (2) Heat Transport: The *Heat Transfer in Fluids* interface models heat transfer in all domains (air, water, infinite
262 element domain) using the following version of the heat equation:

263

$$264 \quad \rho C_p \frac{\partial T}{\partial t} + \rho C_p \mathbf{u} \cdot \nabla T + \nabla \cdot \mathbf{q} = Q_b$$

265

$$\mathbf{q} = -k \nabla T$$

266

267 where ρ (kg/m^3) is the fluid density, C_p ($\text{J}/(\text{kg} \cdot \text{K})$) is the fluid heat capacity at constant pressure, T is the temperature,
268 k ($\text{W}/(\text{m} \cdot \text{K})$) is the fluid thermal conductivity, \mathbf{u} (m/s) is the fluid velocity field from the Laminar Flow interface, \mathbf{q}
269 (W/m^2) is the heat flux by conduction, and Q_b (W/m^3) is the heat sink due to evaporative cooling at the droplet surface.

270

271 (3) Mass transport: The *Transport of Diluted Species* interface models water vapor transport through Fick's laws of
272 diffusion, solving the mass conservation equation for vapor transfer in all domains except within the cloud droplet:

273

$$\frac{\partial c}{\partial t} + \nabla \cdot \mathbf{J} = 0$$

274

$$\mathbf{J} = -D \nabla c$$



275

276 where c is the concentration of water vapor (mol/m^3), D denotes the diffusion coefficient (m^2/s), and \mathbf{J} is the mass flux
277 diffusive flux vector ($\text{mol}/(\text{m}^2\cdot\text{s})$). D is calculated following Hall and Pruppacher (1976) and defined as follows: $D =$
278 $0.0000211 \frac{P_0}{P} \left[\frac{T}{T_0} \right]^{1.94}$ ($\text{m}^2 \text{ s}^{-1}$) with reference pressure, $P_0 = 1013.25$ hPa, reference temperature, $T_0 = 273.15$ K,
279 atmospheric temperature, T , and pressure, P . In this study, values of P are either fixed at 500 or 850 hPa to determine
280 the effect of ambient air pressure on droplet evaporation. \mathbf{J} is obtained from the Laminar Flow interface through
281 coupling between these interfaces.

282

283 3.3 Initial conditions

284

285 The initial velocity components in the r , and z directions are assumed to be 0 m/s in both air and water domains. The
286 initial fluid pressure is $p = P_{0,air}$ (Pa), specified either at 500 or 850 hPa in the air domain, and in the water domain, p
287 $= P_{0,water} = \frac{2\sigma}{r_0}$ Pa, where surface tension, $\sigma = 70 \times 10^{-3}$ (N/m). For the heat transfer module, all domains are assumed
288 to be at a prescribed initial ambient temperature, T_0 , which is the same as that of a point at a far distance away from
289 the droplet, T_∞ . For the vapor transfer interface, except within the droplet, all domains are at an initial vapor
290 concentration of $c_{0,air}$ which is again assumed to be the same as that of the constant ambient concentration value far
291 from the droplet, c_∞ , calculated as follows:

292 $c_\infty = \frac{RH_\infty \times e_{sT_\infty}}{R_{univ} \times T_\infty}$ where, RH_∞ is set at a constant ambient relative humidity far from the droplet, $R_{univ} = 8.3145$ (J/mol/K)

293 and saturation vapor pressure, $e_{sT_\infty} = 610.94 * \exp\left(\frac{17.625 * T_\infty}{T_\infty + 243.04}\right)$ (in Pa, with T_∞ in °C) following Alduchov and
294 Eskridge (1996).

295

296

297 3.4 Boundary Conditions

298

299 1. At the center of the domain, $r = 0$, axisymmetric conditions are applicable:

300

301

$$\mathbf{u} \cdot \mathbf{n} = 0$$

302

$$[-p\mathbf{I} + \boldsymbol{\tau}] \cdot \mathbf{n} = 0$$

303

$$\mathbf{q} \cdot \mathbf{n} = -k\nabla T \cdot \mathbf{n} = 0$$

304

$$-D\nabla c \cdot \mathbf{n} = 0$$

305 where \mathbf{n} is the outward-pointing surface normal vector.

306

307 2. At the fluid-fluid interface i.e., droplet-air boundary, the droplet surface is assumed to be at vapor saturation
308 throughout its lifetime. Hence, saturated vapor concentration at the shrinking droplet boundary, using the ideal gas



309 law, is given by, $c_{sat}(T_{sf}) = \frac{e_s(T)}{R_{univ} \times T}$ where saturation vapor pressure, $e_s(T)$, is estimated following Alduchov and
 310 Eskridge (1996) at $T = T_{sf}$, the temperature at the droplet surface (in °C).

311

312 The local evaporative mass flux at the interface is given by diffusion of water vapor across the water-air interface, M_J
 313 (kg/ m² s)

$$314 \quad M_J = M_w \mathbf{n} \cdot (-D \nabla c)$$

315

316 where the molecular weight of water, $M_w = 0.018$ (kg/mol). Although the temperature is continuous across the droplet-
 317 air boundary, there is a discontinuity in heat flux across the interface due to the evaporation of water. Thus, the latent
 318 heat of evaporation L , defined as $L = [2501 - 2.44T_r]$ kJ kg⁻¹ with droplet surface temperature, T_r in °C, is
 319 incorporated as a boundary heat sink as $-M_J L$ (W/m²).

320

321 The mass balance at the water-vapor boundary at the droplet surface, and the velocity of the moving mesh \mathbf{u}_{mesh} , at
 322 the shrinking water-air interface, are expressed by the following equations, based on Scardovelli and Zaleski, (1999):

323

$$324 \quad \mathbf{u}_w = \mathbf{u}_v + M_J \left(\frac{1}{\rho_w} - \frac{1}{\rho_v} \right) \mathbf{n}$$

325

$$326 \quad \mathbf{u}_{mesh} = \left(\mathbf{u}_w \cdot \mathbf{n} - \frac{M_J}{\rho_w} \right) \mathbf{n}$$

327

328 where the subscripts w and v represent water and vapor respectively.

329

330 The stresses are balanced at the water-vapor interface by the following conditions:

331

$$332 \quad \mathbf{n} \cdot (\mathbf{S}_w - \mathbf{S}_v) = \sigma (\nabla_\sigma \cdot \mathbf{n}) \mathbf{n} - \nabla_\sigma \sigma$$

333

$$\mathbf{S} = [-p\mathbf{I} + \boldsymbol{\tau}]$$

334

335 where \mathbf{S} is the total stress tensor and ∇_σ is the surface gradient operator defined by

336

$$337 \quad \nabla_\sigma = (\mathbf{I} - \mathbf{n} \cdot \mathbf{n}^T) \nabla$$

338

339 In the normal direction of the boundary, the force is balanced by,

340

$$341 \quad \mathbf{n} \cdot (\mathbf{S}_w - \mathbf{S}_v) = \frac{\sigma}{r_c} \cdot \mathbf{n}$$

342



343 where r_c is the curvature radius.

344

345 3. The external air domain boundary is open with the following condition:

346 $[-\mathbf{p}\mathbf{I} + \boldsymbol{\tau}]\mathbf{n} = -f_0\mathbf{n}$, where normal stress, $f_0 = 0 \text{ N/m}^2$.

347

348 4. The infinite element domain consists of air and is considered to be an ideal gas. The temperature, relative humidity,
349 and concentration far from the droplet i.e., at the inner boundary of the infinite element domain, are fixed at T_∞ and
350 c_∞ , respectively.

351

352 **3.5 Coupling between the COMSOL interfaces**

353

354 To numerically model the evaporating droplet embedded in the air domain, intercoupling between the three physics
355 interfaces - laminar two-phase flow (formulated within the Arbitrary Lagrangian-Eulerian framework), the heat
356 transfer in fluids, and the transport of diluted species within the air medium are established through the following
357 mechanisms: (i) the local evaporative mass flux at the droplet-air interface, which is related to the mesh velocity for
358 the laminar flow, is estimated by the diffusion of water vapor in the air domain; (ii) saturated vapor concentration at
359 the droplet-air interface, which serves as a boundary condition for the vapor diffusion, is calculated using the local
360 temperature at the droplet interface; and (iii) the evaporative heat flux at the droplet-air interface acts as a heat sink
361 boundary condition for the heat transfer in fluids module.

362

363 **4 Results**

364

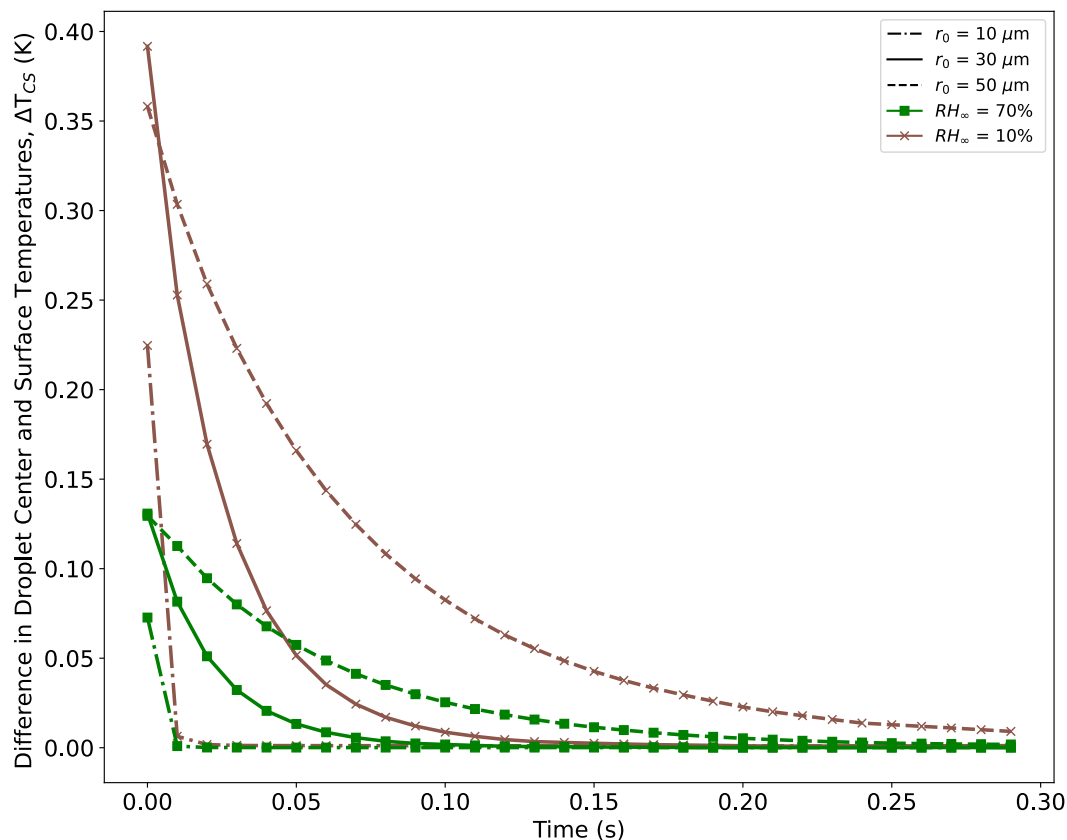
365 **4.1 Internal Droplet Temperature Evolution**

366

367 Since evaporation is a surface phenomenon, with the evaporative cooling at the droplet surface acting as a heat sink,
368 the temperature of the evaporating droplet surface should be lower than the center of the droplet. This is indeed the
369 case, as shown in the examples in Fig. 3, where 10, 30 and 50 μm droplets are evaporating in two types of
370 environments: very dry ($RH_\infty = 10\%$) and relatively moist ($RH_\infty = 70\%$), with $P = 500 \text{ hPa}$, and $T_\infty = 273.15 \text{ K}$. Note
371 that the center to surface temperature gradient within the droplet forms almost instantaneously ($<$ smallest output
372 timestep of 0.01 s) as evaporative cooling at the droplet surface occurs extremely fast. The time required for the droplet
373 to reach internal thermal equilibrium depends slightly on the initial size of the droplet and the ambient RH_∞ , with
374 larger droplets and drier environments leading to more time required by the droplets to reach equilibrium. However,
375 generally, for typical cloud droplet sizes and environmental conditions considered here ($r_0 = 10, 30, 50 \mu\text{m}$), the
376 internal thermal gradients dissipate and the temperatures throughout the droplets become uniform in $\leq 0.3 \text{ s}$. This can
377 be explained by the high thermal conductivity values of water (assumed constant at 0.556 W/(m K)) and the absence
378 of any heat source within the droplet. For this study, we have simulated internal droplet heat transfer for the entirety



379 of the droplet lifetime and will be reporting the average droplet temperatures as “droplet temperatures” in the results,
380 unless noted otherwise.
381



382
383 **Figure 3: Thermal evolution of the temperature difference between the droplet center and surface temperatures, ΔT_{CS}**
384 **(K), for $r_0 = 10, 30$ and $50 \mu\text{m}$, for two kinds of environments – dry ($RH_{\infty} = 10\%$, brown curves) and relatively moist (RH_{∞}**
385 **$= 70\%$, green curves), with $P = 500 \text{ hPa}$, $T_{\infty} = 273.15 \text{ K}$ (0°C).**

386 4.2 Droplet Thermal and Radial Evolution: Influence of Initial Droplet Size and Environmental Factors

387

388 Figures. 4 and 5 depict the evolution of the droplet average temperatures and radii ($r_0 = 10, 30$ and $50 \mu\text{m}$) for the first
389 10 seconds of their lifetimes (as defined in Sec. 2c), for different environments with constant ambient conditions (T_{∞} ,
390 RH_{∞} , and P) far from the droplet. These figures also visually summarize droplet temperatures at the end of their
391 lifetimes (T_L) and the total lifetimes of the droplets (t_L). For all numerical experiments, the evaporating droplet
392 temperature decreases sharply, within $< 0.5 \text{ s}$, to a certain temperature defined here as the inflection point in the curves,
393 T_i (see discussion in Sec. 4c and Sec. 5a). After reaching T_i , the decrease in droplet temperature is relatively more
394 gradual as can be seen from Figs. 4 and 5. For example, in Fig. 4(c), for $P = 500 \text{ hPa}$, $T_{\infty} = 268.15 \text{ K}$ (-5°C), $RH_{\infty} =$
395 10% , a droplet with $r_0 = 10 \mu\text{m}$, takes about 0.03 s to reach T_i , at 260.98 K (a decrease of 7.17 K from initial



396 temperature, with a mean cooling rate of 239 K s^{-1}). In contrast, a $30 \mu\text{m}$ droplet takes about 0.12 s to reach T_i at
397 260.85 K (a decrease of 7.3 K from initial temperature, with a mean cooling rate of 60.83 K s^{-1}), and a $50 \mu\text{m}$ droplet
398 takes about 0.33 s to reach T_i (with a mean cooling rate of 22.12 K s^{-1}). Finally, the $10 \mu\text{m}$ droplet reaches the end of
399 its lifetime in 1.05 s i.e. $t_L = 1.05 \text{ s}$ with temperature, $T_L = 244.12 \text{ K}$, with a mean cooling rate of 16.52 K/s after
400 reaching T_i , while for the $30 \mu\text{m}$ droplet, $t_L = 11.4 \text{ s}$ with $T_L = 244.31 \text{ K}$ (mean cooling rate of 1.47 K/s after reaching
401 T_i), and $t_L = 32.76 \text{ s}$ for the $50 \mu\text{m}$ droplet with $T_L = 244.29 \text{ K}$, with a mean cooling rate of 0.51 K/s after reaching T_i .
402

403 In general, we can see that a higher ambient T_∞ , and lower RH_∞ and P leads to a larger reduction in droplet temperature
404 from its initial temperature. Therefore, drier, relatively warmer (closer to 0°C), and lower-pressure environments lead
405 to the strongest evaporative cooling of the droplets. Also, due to evaporative cooling, the droplets survive longer as
406 compared to the pure diffusion-limited evaporation approach where the decreases in evaporating droplet temperature
407 have not been considered (see Sec. 5). However, drier, relatively warmer (close to 0°C), and lower-pressure
408 environments lead to smaller droplet lifetimes as compared to more humid environments, with lower ambient
409 temperatures and higher pressures.

410

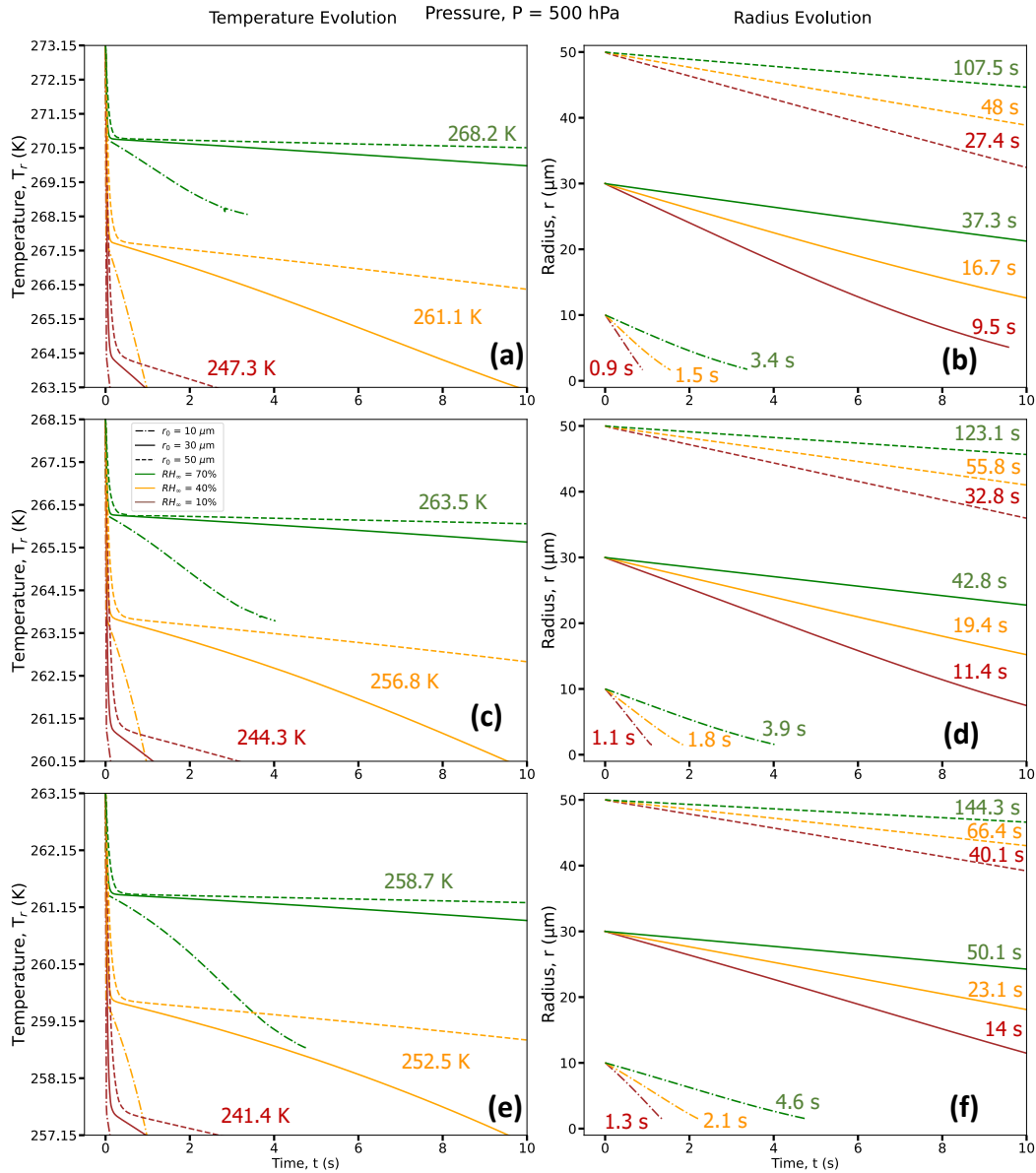
411 **4.3 Environmental Evolution: Evolution of Temperature, Relative Humidity, and Wet-Bulb Temperature in** 412 **the Air domain near the droplet**

413

414 Figures. 6-8 (a, d) show radial cross sections of the computational domain, starting from the center of the droplet on
415 the origin of x axis = $0 \mu\text{m}$ to the edge of the domain at $x = 1500 \mu\text{m}$, while Figs. 6-8 (b, e) expand the dashed box
416 regions of Figs. 6-8 (a, d), and Figs. 6-8 (c, f) further expand the dashed box regions of Figs. 6-8 (b, e). All panels
417 show the spatiotemporal evolution of temperature, relative humidity, thermodynamic wet-bulb temperature, and
418 droplet radius for a droplet with initial radius, $r_0 = 50 \mu\text{m}$, introduced to an initial environment with pressure, $P = 500$
419 hPa, ambient temperature, $T_\infty = 268.15 \text{ K}$ (-5°C), with two different relative humidities, $RH_\infty = 10\%$ and 70% . The
420 evolution of temperature within the droplet is left of the dashed black line, which denotes the droplet radius.

421

422 As the droplet evaporates in the subsaturated domain, evaporative cooling occurs at the droplet surface, leading to
423 heat transfer both from within the warmer droplet and the surrounding air to balance the cooling at the droplet surface.
424 Since the droplet has no constant internal heat source, the internal thermal gradients dissipate quite fast (within 0.3 s)
425 and the average droplet temperatures continue to decrease as the droplet evaporates. Due to heat exchange between
426 the droplet surface and the ambient air in its vicinity, transient thermal gradients in the ambient air develop and lead
427 to a decrease in the air temperature near the droplet. As the droplet shrinks in size along with cooling further, the
428 colder envelope of air surrounding the droplet shrinks as well and the ambient air far from the droplet, at a constant
429 temperature, acts as a heat source and supplies heat to the rest of the domain to equilibrate the air temperature.
430 Comparing Fig. 6 (a) and (d), at the lower RH_∞ , the magnitude of evaporative cooling is much higher. For example,
431 the average temperature of the $50 \mu\text{m}$ droplet decreases by $\sim 10 \text{ K}$ in 9 s when $RH_\infty = 10\%$, while the decrease is ~ 5
432 K in 120 s , when $RH_\infty = 70\%$.



433

434

435

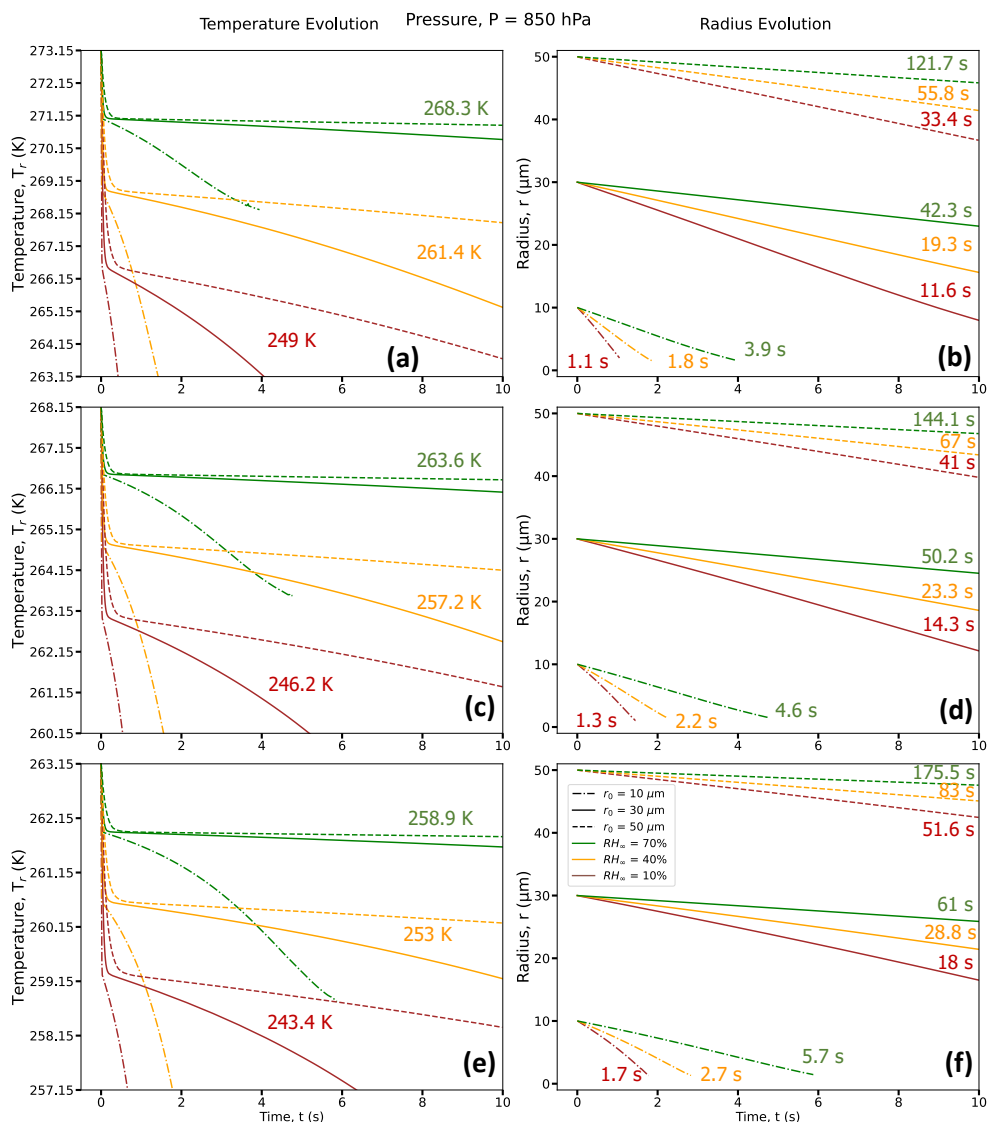
436

437

438

439

Figure 4: Droplet temperature evolution (left column) and radius evolution (right column) for three different RH_∞ ($RH_\infty = 10\%$ (brown curves), 40% (orange curves) and 70% (green curves)), three different r_0 ($r_0 = 10$ μm (dot-dashed lines), 30 μm (solid lines) and 50 μm (dashed lines)), with three different $T_\infty = 273.15$ K (0°C) (a, b), 268.15 K (-5°C) (c, d) and 263.15 K (-10°C) (e, f), for $P = 500$ hPa. For each RH_∞ , the droplet temperature at the end of its lifetime (T_L , in K) is given in (a,c,e) and the time taken to reach the end of its lifetime (t_L , in s) is given in (b,d,f).

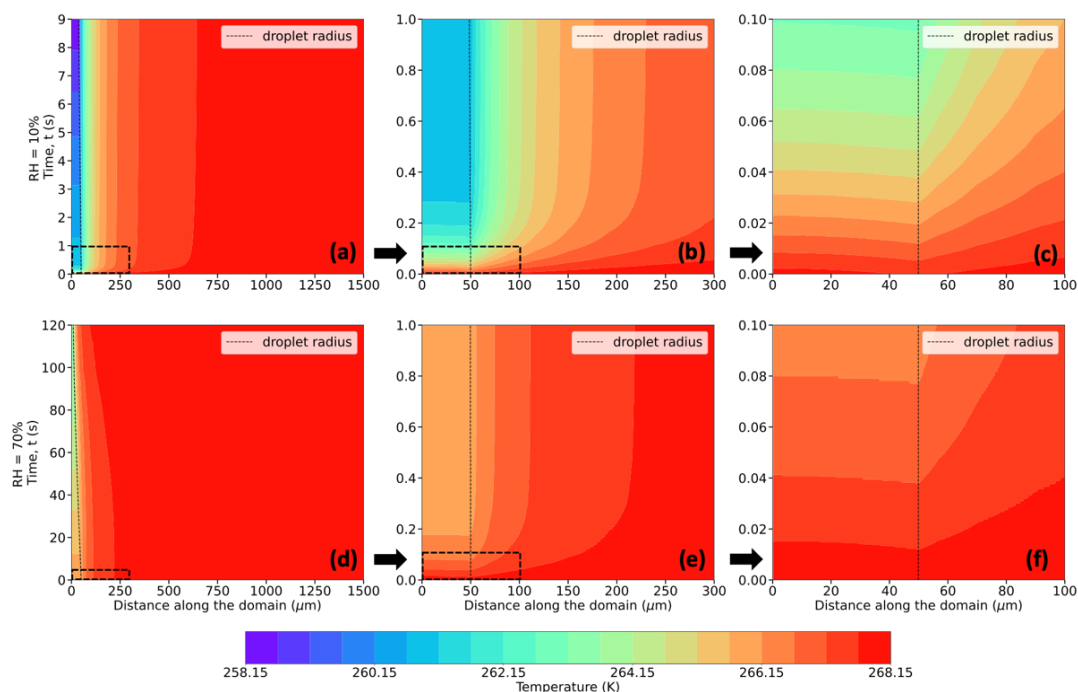


440

441 **Figure 5: Same as Fig. 4 but for $P = 850$ hPa.**

442 In these simulations, the air in contact with the droplet surface is saturated with respect to water, i.e., $RH = 100\%$ (Fig.
 443 7, a-f), consistent with assumptions of isolated, stationary evaporating droplets (Kinzer and Gunn, 1951; Srivastava
 444 and Coen, 1992). As the water vapor from the evaporating droplet surface diffuses into the surrounding environment,
 445 with an initial RH (same as RH_∞) of say 10%, vapor density gradients, similar to the thermal gradients, appear and
 446 impact the immediate environment of the droplet. These spatiotemporally varying thermal and vapor density gradients
 447 play an important role in affecting the droplet temperatures, evaporation rates, and in turn, droplet lifetimes.

448



449

450

451

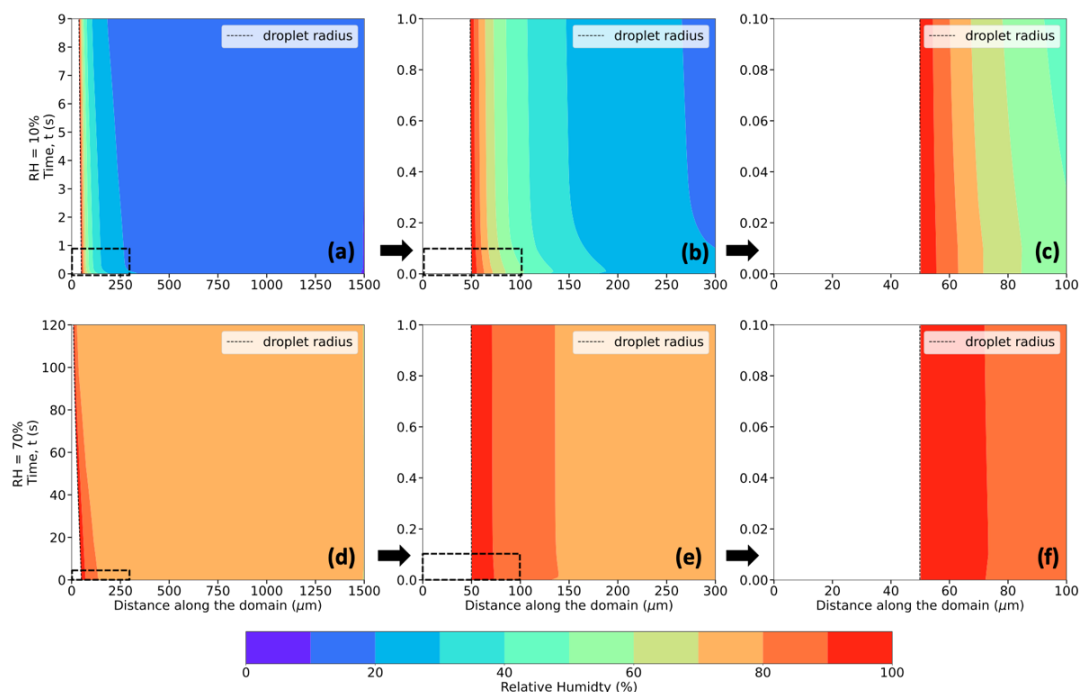
452

453

Figure 6: Evolution of temperature (in K, shaded contours), and droplet radius (in μm , dashed black trace) for a $50 \mu\text{m}$ droplet, immersed in an environment with $T_{\infty} = 268.15 \text{ K}$ (-5°C), $P = 500 \text{ hPa}$, and $RH_{\infty} = 10\%$ (top row) and 70% (bottom rows). Figures denoted as (b) and (e), and (c) and (f) present zoomed-in plot areas marked by the dashed boxes in (a) and (d), and (b) and (e), respectively.



454



455

456

Figure 7: Same as Figure 6, but for Relative Humidity (in %, shaded contours), instead of Temperature.

457

458

459

460

461

462

463

464

465

466

467

468

469

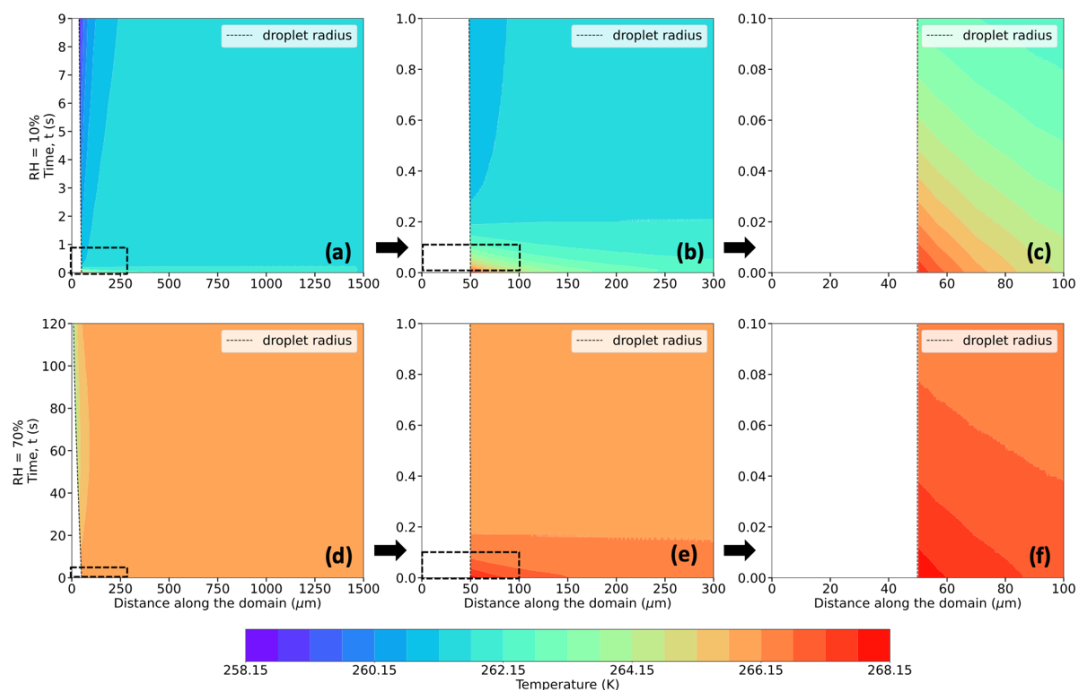
470

471

472

473

Roy et al. (2023) has shown that an evaporating cloud droplet temperature can be well-approximated by the thermodynamic wet-bulb temperature of the environment, especially at higher relative humidities and pressures, and lower ambient temperatures. Following the iterative procedure used in Roy et al. (2023) to calculate the thermodynamic wet-bulb temperature (T_{WB}), Fig. 8 (a-f) depicts the evolution of T_{WB} of the surrounding environment. Unlike previous studies (Srivastava and Coen, 1992; Roy et al., 2023), the ambient environment in this study is not assumed to be spatiotemporally invariant. Hence, as the thermal and vapor density gradients evolve in the ambient air, the T_{WB} of the environment evolves as well, depending on the temperature, relative humidity, and pressure, with the droplet surface temperature the same as that of the T_{WB} of its immediate environment at all times. Of interest, the droplet temperature decreases very quickly to T_i within < 0.5 s (Figs. 4 and 5), which agrees very well with the initial T_{WB} of the surrounding environment and the constant value of the thermodynamic wet bulb temperature far from the droplet ($T_{WB\infty}$). For example, in Fig. 8(a-c), $T_\infty = 268.15$ K, $P = 500$ hPa, $RH_\infty = 10\%$, $T_{WB\infty} = 261.64$ K, and in Fig. 8(d-f), for $RH_\infty = 70\%$, $T_{WB\infty} = 266.13$ K. Fig. 8 shows the two phases of the evolution of T_{WB} of the immediate environment for two RH_∞ environments – initially, there is a very fast decrease of the air temperature at the droplet surface to $T_{WB\infty}$ typically within < 0.3 s, and then a more gradual decrease of T_{WB} at the droplet surface as the thermal and vapor density gradients in the ambient air become relatively steadier and more established for a period of time, and as their spheres of influence start shrinking as the droplet starts getting smaller in size.



474

475

Figure 8: Same as Figure 6, but for thermodynamic wet-bulb temperature (in K, shaded contours).

476

477 4.4 Influence of initial droplet size and ambient environmental factors on the thermal evolution of the droplet 478 and its surrounding environment

479

480 To capture the overall trends spanning most of the parameter space, Figs. 9-14 and Tables 1-2 summarize the results
481 from 54 numerical experiments, using various combinations of ambient conditions (RH_∞ , T_∞ , and pressure, P , and r_0)
482 specified at a distance far away from the droplet.

483

484 4.4.1 Effect of Ambient Relative Humidity, RH_∞

485

486 The decrease in droplet temperature is larger when the RH_∞ is lower due to higher evaporation rates and stronger
487 evaporative cooling under drier conditions. For instance, as shown in Table 1 and Fig. 9 (a, b, c), 30 μm droplets reach
488 ~ 247.3 K (a decrease of 25.8 K from the initial temperature of 273.15 K) for $RH_\infty = 10\%$, ~ 261.1 K (a decrease of
489 12.1 K) for $RH_\infty = 40\%$ and ~ 268.2 K (a decrease of ~ 5 K) for $RH_\infty = 70\%$. The droplet lifetimes vary widely
490 depending on RH_∞ , with lifetimes increasing with an increase in humidity. For example, the droplet lifetimes for the
491 30 μm droplet are ~ 9.5 s, 16.7 s, and 37.3 s for environments with $RH_\infty = 10\%$, 40% and 70%, respectively (Table
492 2). The decrease in droplet temperature and increase in droplet lifetime show similar dependence with increasing RH_∞
493 for 10 and 50 μm droplets as well.



494 **4.4.2 Effect of Initial Droplet Size, r_0**

495

496 From Figs. 9-14, the decrease in droplet temperatures is independent of the initial droplet size if all other initial
497 environmental conditions are kept constant. For example, from Table 1 and Fig. 10 (a-i) at $P = 500$ hPa, 10, 30 and
498 $50 \mu\text{m}$ droplets reach ~ 244 K (a decrease of ~ 24 K from the initial temperature of 268.15 K) for $RH_\infty = 10\%$, ~ 256.8
499 K for $RH_\infty = 40\%$, and ~ 263.5 K for $RH_\infty = 70\%$. On the other hand, the droplet lifetime strongly depends on the
500 initial droplet size, as the larger droplets take more time to evaporate as compared to the smaller ones. For
501 environments with $RH_\infty = 10\%$, 40% and 70% , the droplet lifetimes for the $10 \mu\text{m}$ droplet are ~ 1.1 s, 1.8 s, and 3.9 s,
502 while for the $30 \mu\text{m}$ droplet are ~ 11.4 s, 19.4 s, and 42.8 s, and for the $50 \mu\text{m}$ droplet are ~ 32.8 s, 55.8 s, and 123.1
503 s, respectively (Table 2). For a higher pressure of $P = 850$ hPa (Table 1 and Fig. 13a-i), at the same T_∞ , irrespective
504 of r_0 , the decrease in droplet temperatures is slightly smaller as compared to $P = 500$ hPa, with values of 22 K, 11 K,
505 and 4.6 K. The nature of these dependencies on r_0 is in good agreement with those reported in Roy et al., (2023). The
506 radial dependence of the thermal gradients in the ambient air also depends on the initial droplet size, decreasing with
507 a decrease in r_0 .

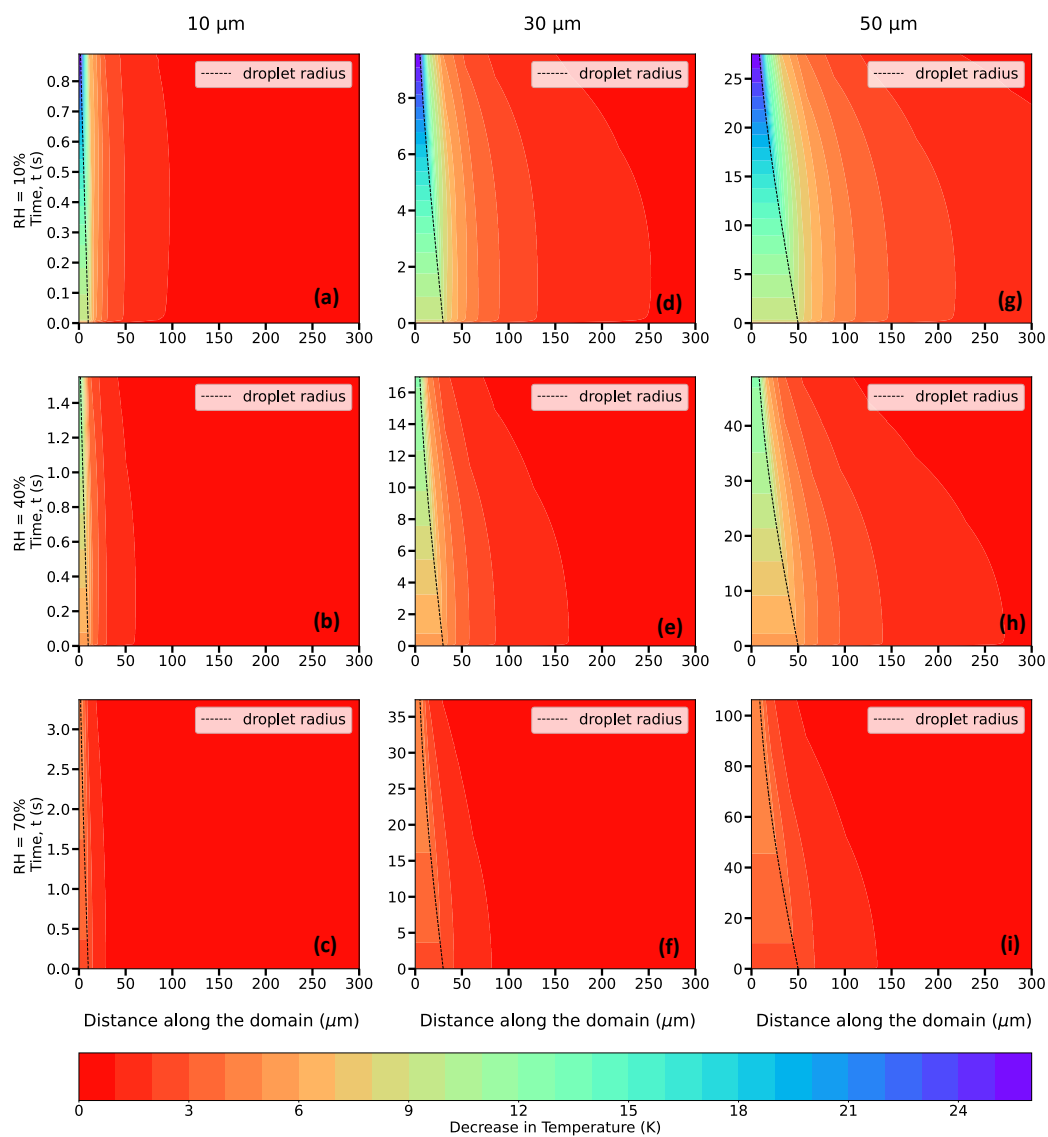
508

509 **4.4.3 Effect of Ambient Temperature, T_∞**

510

511 To determine the effect of a lower ambient temperature on droplet temperatures and lifetimes, Figs. 10 and 11
512 demonstrate similar plots as shown in Fig. 9, but for $T_\infty = 268.15$ K (-5°C) and 263.15 K (-10°C), respectively. The
513 decrease in droplet temperatures and increase in droplet lifetimes depict similar relationships with RH_∞ and r_0 .
514 Droplets, irrespective of their initial size, cool to a lower temperature depending on the ambient RH_∞ , with the
515 magnitude of the cooling being inversely proportional to the subsaturation of the ambient environment. For instance,
516 for 10 , 30 and $50 \mu\text{m}$ droplets, from an initial temperature of 268.15 K, the droplet temperatures approximately
517 decrease by 24 K, 11.4 K, and 4.7 K, for environments with $RH_\infty = 10\%$, 40% , and 70% , respectively (Table 1). The
518 droplet lifetimes for the $10 \mu\text{m}$ droplet are ~ 1.1 s, 1.8 s, and 3.9 s, while for the $30 \mu\text{m}$ droplet are ~ 11.4 s, 19.4 s,
519 and 42.8 s, and for the $50 \mu\text{m}$ droplet are ~ 32.8 s, 55.8 s, and 123.1 s, for $RH_\infty = 10\%$, 40% and 70% , respectively
520 (Table 2). Comparing these values with those of $T_\infty = 273.15$ K (0°C), it can be noted that a lower ambient temperature
521 leads to a smaller decrease in droplet temperatures and a slight increase in droplet lifetimes in a spatiotemporally
522 evolving environment, for the same RH_∞ , r_0 and P , as shown by Roy et al., 2023. Fig. 11 and Table 1 depict that for
523 $T_\infty = 263.15$ K (-10°C), the reduction in droplet temperatures is slightly smaller, ~ 21.8 K, 10.7 K, and 4.5 K for
524 environments with $RH_\infty = 10\%$, 40% , and 70% , respectively, and droplet lifetimes are longer relative to the higher
525 ambient temperatures of 273.15 K and 268.15 K (Table 2). This is because at a lower ambient temperature, the vapor
526 diffusivity into the ambient air is lower, leading to a weaker evaporation rate with slightly reduced cooling, and
527 extended droplet lifetime, relative to those in an environment with a higher ambient temperature.

528



529
 530
 531
 532
 533
 534
 535
 536
 537
 538
 539
 540

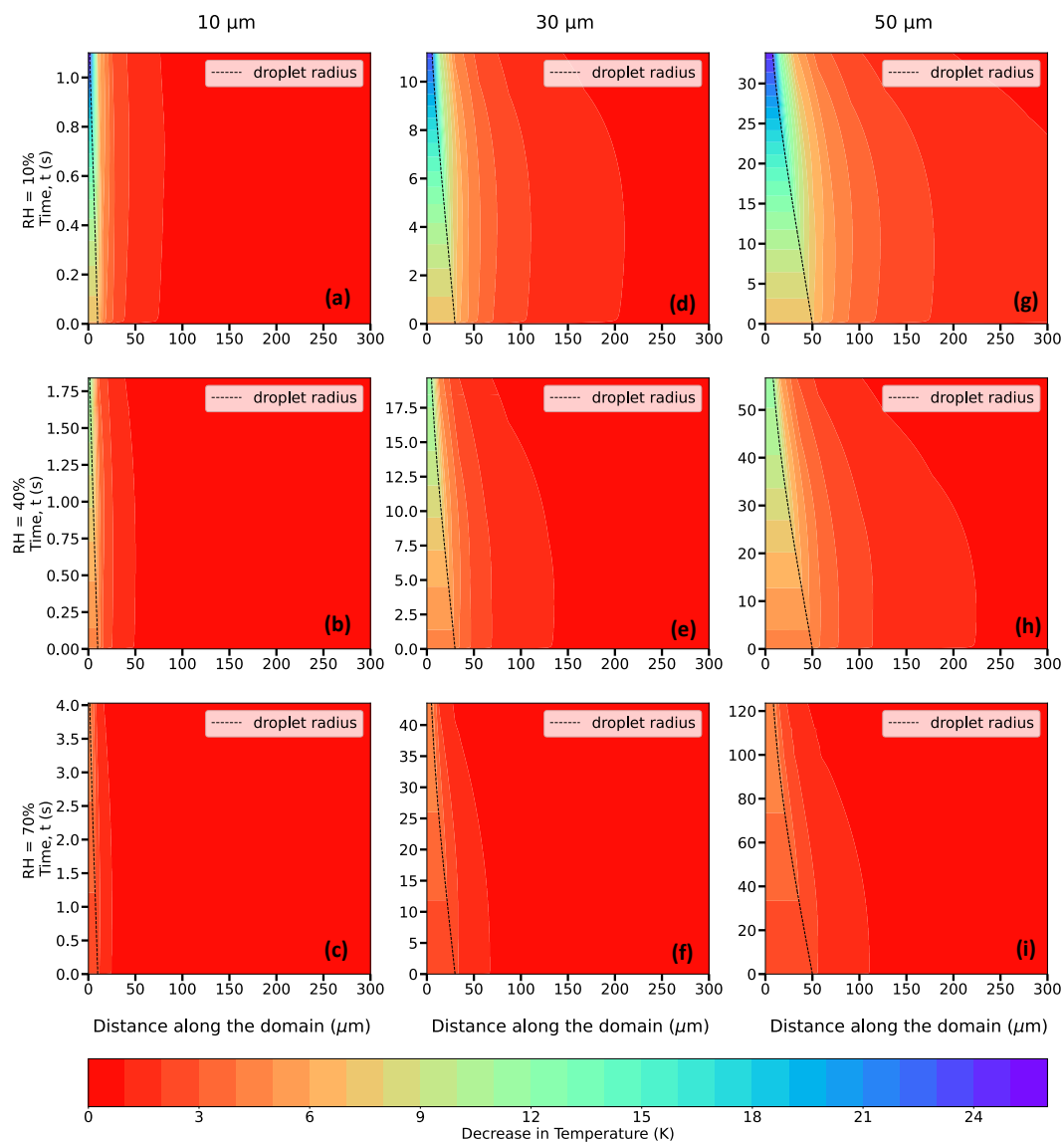
Figure 9: Evolution of the decrease in temperature (in K, shaded contours) from the initial temperature of the domain = 273.15 K (0°C), and of the droplet radius (in μm, dashed black trace) for 10 (a,b,c), 30 (d,e,f), and 50 (g,h,i) μm droplets, immersed in an environment with $T_{\infty} = 273.15$ K (0°C), $P = 500$ hPa, and $RH_{\infty} = 10\%$, 40% and 70% .



T_{∞} (K)	r_0 (μm)	RH_{∞} (%)	$P = 500 \text{ hPa}$					$P = 850 \text{ hPa}$				
			$T_{WB\infty}$ (K)	T_{RRD} (K)	T_i (K)	T_L (K)	$T_{\infty} - T_L$ (K)	$T_{WB\infty}$ (K)	T_{RRD} (K)	T_i (K)	T_L (K)	$T_{\infty} - T_L$ (K)
273.15 (0°C)	10	10	264.94	264.06	264.15	247.15	26	267.20	266.49	266.35	249.03	24.12
		40	267.95	267.41	267.35	261.09	12.06	269.30	268.85	268.95	261.40	11.75
		70	270.67	270.43	270.35	268.21	4.94	271.28	271.07	271.10	268.29	4.86
	30	10	264.94	264.06	264.15	247.33	25.82	267.20	266.49	266.37	249.01	24.14
		40	267.95	267.41	267.35	261.08	12.07	269.30	268.85	268.95	261.43	11.72
		70	270.67	270.43	270.45	268.20	4.95	271.28	271.07	271.15	268.26	4.89
	50	10	264.94	264.06	264.15	247.31	25.84	267.20	266.49	266.37	249.04	24.11
		40	267.95	267.41	267.36	261.09	12.06	269.30	268.85	268.95	261.45	11.7
		70	270.67	270.43	270.45	268.20	4.95	271.28	271.07	271.15	268.29	4.86
268.15 (-5°C)	10	10	261.64	260.90	260.98	244.12	24.03	263.57	263.01	263.15	246.32	21.83
		40	263.96	263.50	263.48	256.77	11.38	265.16	264.79	264.82	257.17	10.98
		70	266.13	265.91	265.9	263.47	4.68	266.68	266.51	266.65	263.57	4.58
	30	10	261.64	260.90	260.85	244.31	23.84	263.57	263.01	263.06	246.18	21.97
		40	263.96	263.50	263.46	256.76	11.39	265.16	264.79	264.69	257.18	10.97
		70	266.13	265.91	265.92	263.47	4.68	266.68	266.51	266.56	263.58	4.57
	50	10	261.64	260.90	260.85	244.29	23.86	263.57	263.01	263.06	246.21	21.94
		40	263.96	263.50	263.47	256.76	11.39	265.16	264.79	264.72	257.16	10.99
		70	266.13	265.91	265.92	263.46	4.69	266.68	266.51	266.56	263.56	4.59
263.15 (-10°C)	10	10	258.14	257.55	257.53	241.38	21.77	259.73	259.28	259.28	243.49	19.66
		40	259.89	259.51	259.65	252.46	10.69	260.90	260.60	260.65	252.97	10.18
		70	261.56	261.38	261.4	258.73	4.42	262.04	261.90	261.90	258.88	4.27
	30	10	258.14	257.55	257.62	241.36	21.79	259.73	259.28	259.28	243.27	19.88
		40	259.89	259.51	259.56	252.47	10.68	260.90	260.60	260.54	252.99	10.16
		70	261.56	261.38	261.39	258.73	4.42	262.04	261.90	261.91	258.88	4.27
	50	10	258.14	257.55	257.62	241.37	21.78	259.73	259.28	259.28	243.48	19.67
		40	259.89	259.51	259.56	252.47	10.68	260.90	260.60	260.56	252.99	10.16
		70	261.56	261.38	261.39	258.73	4.42	262.04	261.90	261.91	258.87	4.28

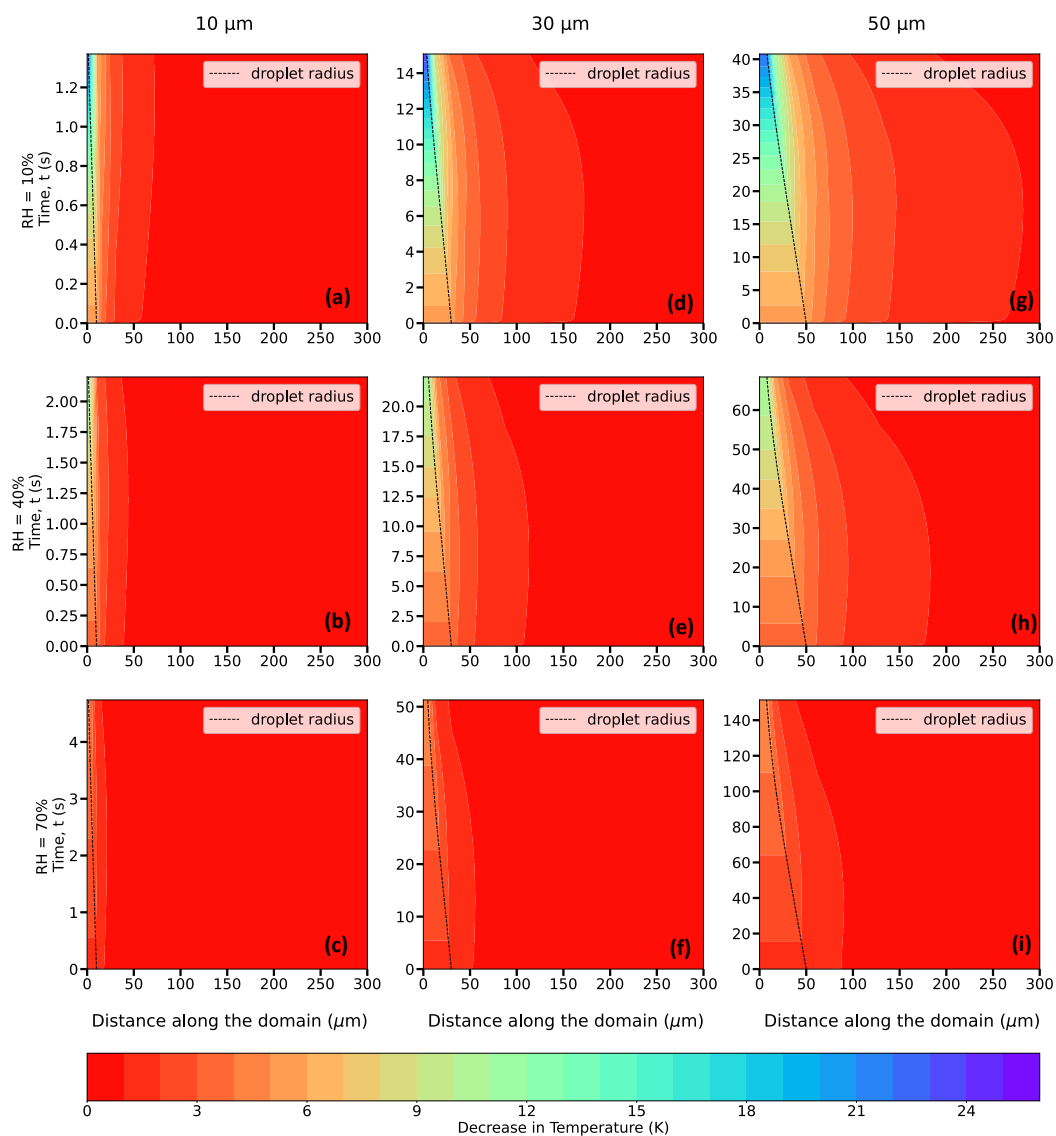


541 **Table 1.** Comparison between thermodynamic wet bulb temperatures in the environment far away from the droplet
 542 ($T_{WB\infty}$), simulated droplet steady-state temperatures from Roy et al., (2023) (T_{RRD}), inflection point temperatures (T_i), and
 543 droplet temperatures at the end of their lifetimes from this study (T_L), in K, for initial droplet radii, $r_0 = 10, 30$ and $50 \mu\text{m}$,
 544 relative humidities, $RH_\infty = 10, 40, 70\%$, and pressures, $P = 500$ and 850 hPa, and ambient temperature, $T_\infty = 273.15$ K (0°C),
 545 268.15 K (-5°C) and 263.15 K (-10°C).
 546



547
 548 **Figure 10:** Same as Fig. 9 but for $T_\infty = 268.15$ K (-5°C).

549



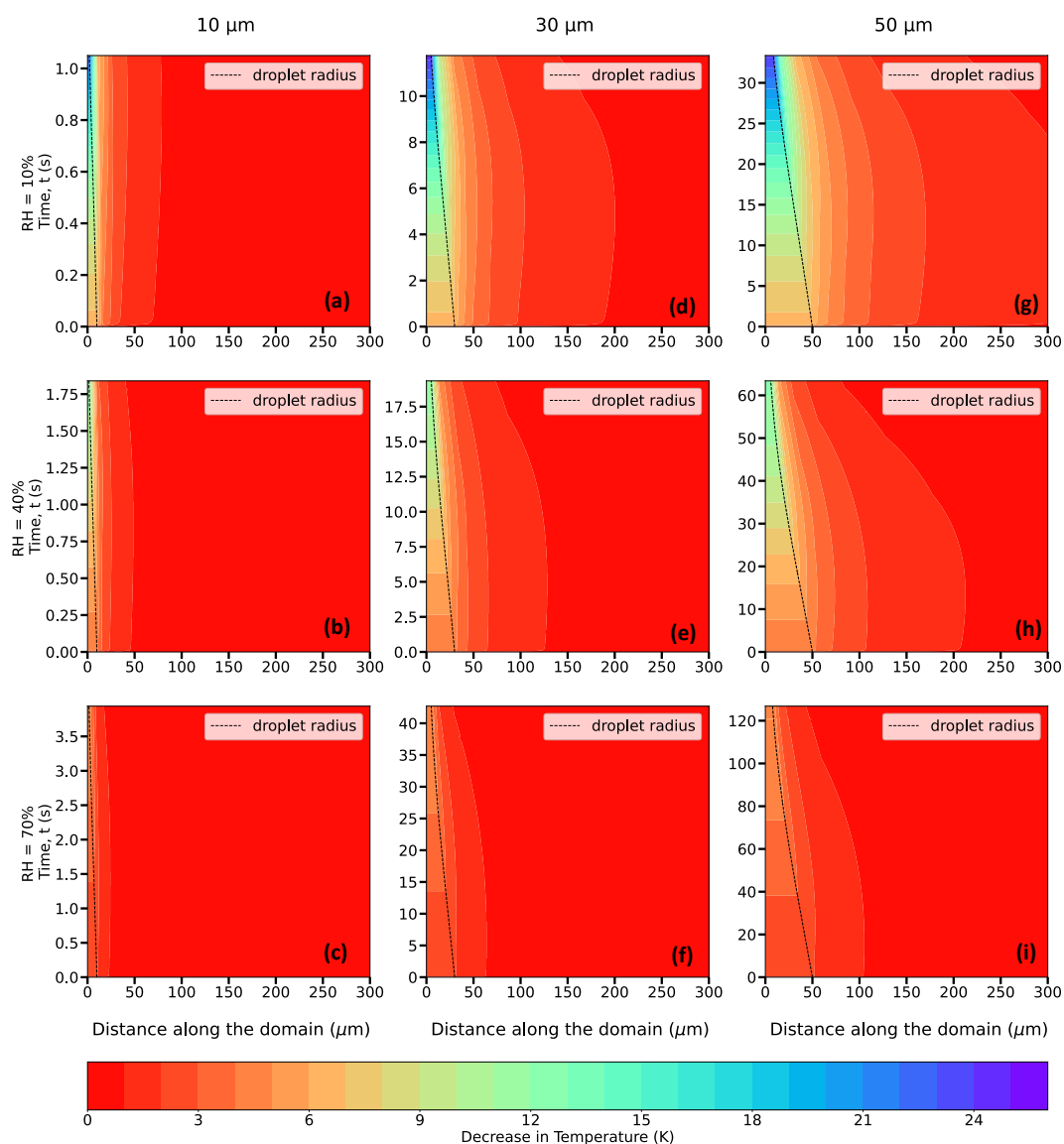
550
 551 **Figure 11: Same as Fig. 9 but for $T_{\infty} = 263.15$ K (-10°C).**

552
 553 **4.4.4 Effect of Ambient Pressure, P**

554
 555 Figures. 12-14 depict the spatiotemporal evolution of the temperature and droplet radius similar to the previous figures,
 556 but now for a higher ambient pressure, $P = 850$ hPa, instead of 500 hPa as shown in Figs. 9-11. For a higher pressure,
 557 the corresponding decreases in droplet temperatures are smaller and droplet lifetimes are longer. Under the same
 558 environmental conditions but with an increase in ambient pressure, water vapor diffusivity decreases, leading to a
 559 decreased evaporation rate, reduced cooling, and extended droplet lifetimes. For example, for an environment with T_{∞}



560 = 273.15 K (0°C), $P = 850$ hPa (Fig. 12 and Table 1), 10, 30 and 50 μm droplets reach 249.0 K, 261.4 K, and 268.3
 561 K for $RH_\infty = 10\%$, 40% and 70%, respectively, which are slightly higher as compared to the corresponding droplet
 562 temperatures (247.3 K, 261.1 K, and 268.2 K) for $P = 500$ hPa (Table 1). For higher ambient pressures, droplet
 563 lifetimes are also increased due to reduced evaporation rate, with 50 μm droplet now surviving for 33.4 s, 55.8 s, and
 564 121.7 s at $P = 850$ hPa, instead of 27.4 s, 48.0 s, 107.5 s for $P = 500$ hPa for $RH_\infty = 10\%$, 40% and 70%, respectively
 565 (Table 2). Similar trends can also be observed for lower ambient temperatures, 268.15 K and 263.15 K, as shown in
 566 Table 2, and Figs. 10 and 13, and 11 and 14.

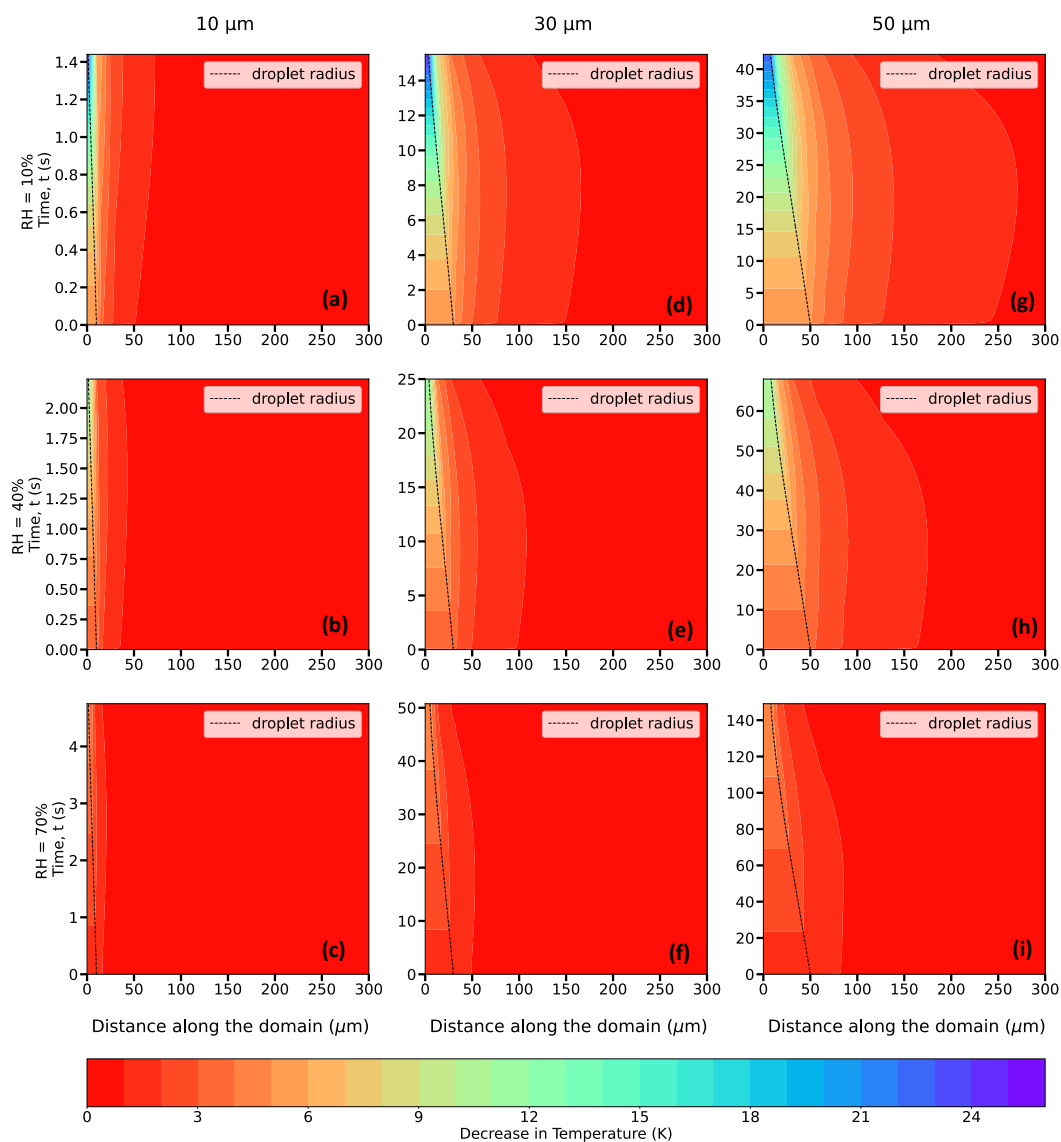


567
 568

Figure 12: Same as Fig. 9 with $T_\infty = 273.15$ K(0°C), but for $P = 850$ hPa.

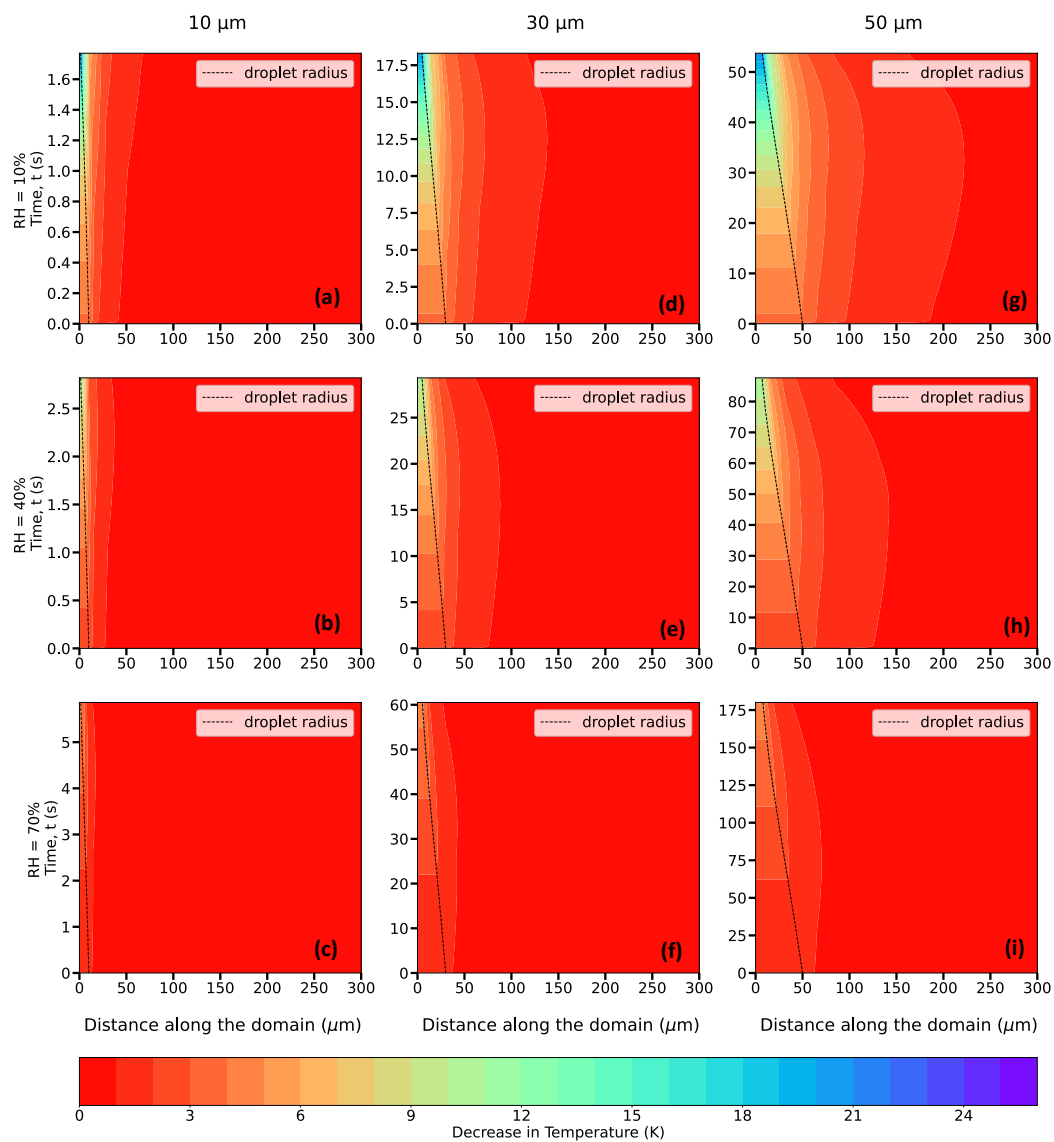


569



570

571 Figure 13: Same as Fig. 12 but for $T_\infty = 268.15 \text{ K}$ (-5°C).



572
573

Figure 14: Same as Fig. 12 but for $T_\infty = 263.15$ K (-10°C).

574
575
576
577
578
579
580
581



T_{∞} (K)	r_0 (μm)	RH_{∞} (%)	$P = 500 \text{ hPa}$				$P = 850 \text{ hPa}$			
			t_{LC} (s)	t_{RRD} (s)	t_L (s)	$t_L - t_{LC}$ (s)	t_{LC} (s)	t_{RRD} (s)	t_L (s)	$t_L - t_{LC}$ (s)
273.15 (0°C)	10	10	0.26	0.56	0.87	0.61	0.44	0.77	1.11	0.67
		40	0.39	0.89	1.51	1.12	0.66	1.18	1.79	1.13
		70	0.78	1.86	3.36	3.36	1.33	2.43	3.87	2.54
	30	10	2.34	5.02	9.54	7.2	3.98	6.84	11.63	7.65
		40	3.51	7.94	16.68	13.17	5.97	10.59	19.33	13.36
		70	7.03	16.73	37.26	30.23	11.95	21.83	42.30	30.35
	50	10	6.51	13.95	27.43	20.92	11.06	19.06	33.35	22.29
		40	9.76	22.08	48.04	38.28	16.59	29.45	55.78	39.19
		70	19.52	46.46	107.45	87.93	33.18	60.64	121.70	88.52
268.15 (-5°C)	10	10	0.38	0.72	1.05	0.67	0.65	1.01	1.32	0.67
		40	0.58	1.12	1.77	1.19	0.98	1.54	2.15	1.17
		70	1.15	2.31	3.91	2.76	1.96	3.14	4.60	2.64
	30	10	3.45	6.42	11.40	7.95	5.87	9.03	14.27	8.4
		40	5.18	10.01	19.35	14.17	8.81	13.83	23.32	14.51
		70	10.36	20.81	42.79	32.43	17.61	28.25	50.15	32.54
	50	10	9.59	17.88	32.76	23.17	16.31	25.15	40.99	24.68
		40	14.39	27.86	55.76	41.37	24.46	38.48	67.02	42.56
		70	28.78	57.80	123.10	94.32	48.92	78.48	144.07	95.15
263.15 (-10°C)	10	10	0.57	0.95	1.29	0.72	0.98	1.37	1.68	0.7
		40	0.86	1.45	2.13	1.27	1.47	2.08	2.68	1.21
		70	1.72	2.98	4.60	2.88	2.93	4.21	5.66	2.73
	30	10	5.17	8.47	13.95	8.78	8.80	12.28	17.99	9.19
		40	7.76	13.05	23.08	15.32	13.19	18.67	28.83	15.64
		70	15.52	26.79	50.12	34.6	26.39	37.85	61.04	34.65
	50	10	14.37	23.59	40.11	25.74	24.43	34.19	51.59	27.16
		40	21.56	36.30	66.42	44.86	36.65	51.93	82.53	45.88
		70	43.12	74.43	144.33	101.21	73.30	105.16	175.50	102.2

582
 583
 584
 585

Table 2: Comparison between different timescales (in sec) in this and other studies, all for the cut off radii used in this study. These include droplet lifetimes using the classical diffusion-limited evaporation approach (t_{LC}), the bulk droplet approach in Roy et al., (2023) (t_{RRD}), and as calculated from this study (t_L), for initial droplet radii ($r_0 = 10, 30$ and $50 \mu\text{m}$),



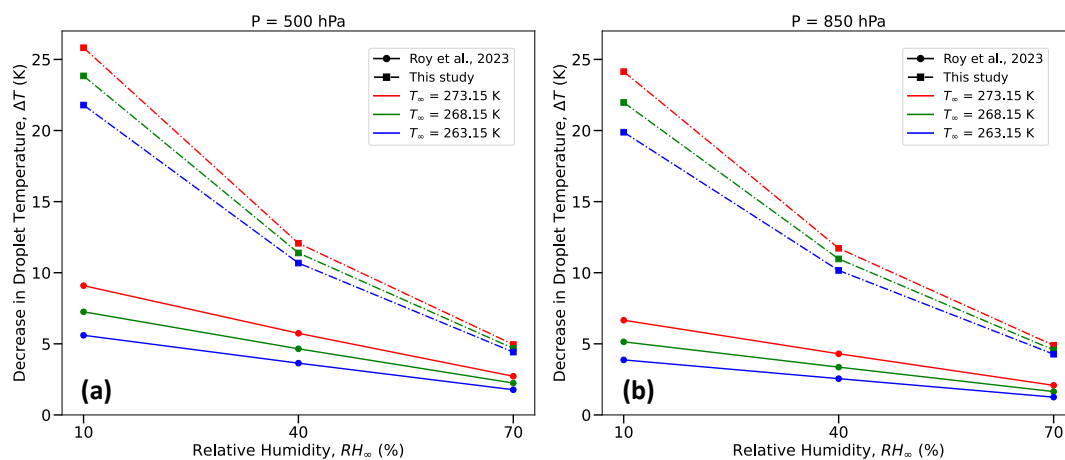
586 relative humidities ($RH_\infty = 10, 40, 70\%$), and pressures ($P = 500$ and 850 hPa), and ambient temperature, $T_\infty = 273.15$ K
 587 (0°C), 268.15 K (-5°C) and 263.15 K (-10°C).
 588

589 5 Discussion

590 5.1 Droplet Temperature and Lifetime Comparison with Previous Studies

591

592 As noted in the introduction, not many studies in the cloud microphysics literature have taken a close look at the
 593 explicit numerical estimation of supercooled, evaporating cloud droplet temperatures for a wide range of
 594 environmental conditions. Previously, a study by Srivastava and Coen (1992) investigated the evaporation of isolated,
 595 stationary droplets by iteratively solving the steady-state solutions, using saturation vapor pressure relations from
 596 Wexler (1976) to calculate saturation vapor density, and assumed the heat storage terms in the droplet heat budget to
 597 be negligible. Solving for time-dependent heat and mass transfer between single, stationary cloud droplets evaporating
 598 in infinitely large, prescribed ambient environments, Roy et al., (2023) demonstrated that the temperatures of the cloud
 599 droplets reach steady-state quite quickly (< 0.5 s). Their steady-state droplet temperatures agreed well with those of
 600 Srivastava and Coen (1992) and could be approximated by the thermodynamic wet-bulb temperature of the ambient
 601 environment. In order to model a more realistic scenario of an isolated droplet evaporating in a subsaturated
 602 environment, the current study advances the idealized framework of droplet evaporation as described in Roy et al.,
 603 (2023) by including the impact of internal heat gradients within the droplet and resolving the spatiotemporally
 604 evolving thermal and vapor density gradients between the droplet and its immediate environment to estimate the
 605 evaporating droplet temperature and lifetime with higher accuracy.



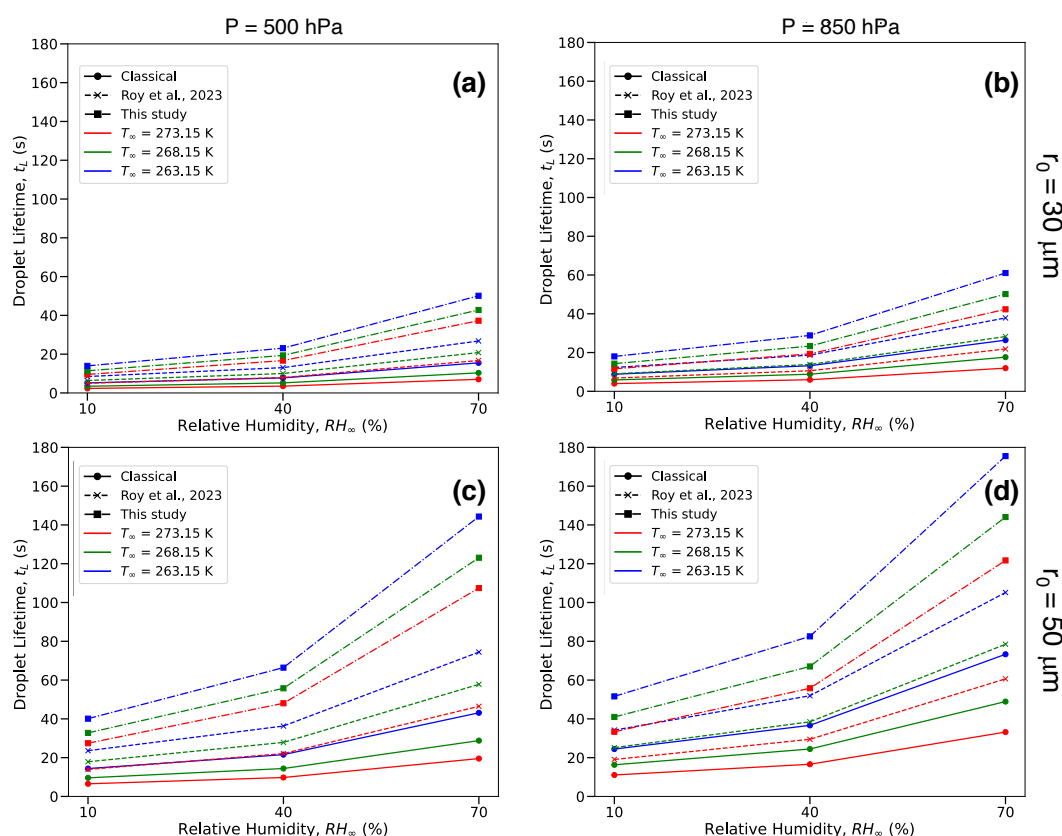
606

607 **Figure 15: Comparison between the decrease in droplet temperatures (in K) from an initial temperature the same as T_∞ ,**
 608 **calculated using the bulk droplet model from Roy et al., (2023) (dashed lines), and this study (dashed-dotted lines), for**
 609 **initial droplet radii, $r_0 = 10, 30$ or $50 \mu\text{m}$, relative humidities ($RH_\infty = 10, 40, 70 \%$), and pressures, $P = 500$ hPa (left column),**
 610 **and 850 hPa right column), and $T_\infty = 273.15$ K (0°C, red), 268.15 K (-5°C, green) and 263.15 K (-10°C, blue).**

611 Table 1 provides a comparison between thermodynamic wet bulb temperatures of the initial environment ($T_{WB\infty}$),
 612 simulated droplet steady-state temperatures from Roy et al. (2023) (T_{RRD}), and droplet temperatures at the end of their
 613 lifetimes from this study (T_L), in K for several environments. Interestingly, the temperatures at the inflection point, T_i ,



614 as defined in Sec. 3e, are in excellent agreement with $T_{WB\infty}$ and T_{RRD} . In the current study, the droplet temperature
 615 continues to decrease almost steadily as the immediate environment in the vicinity of the droplet cools, finally reaching
 616 T_L , unlike the evaporating droplet achieving steady-state temperature in a prescribed ambient environment far away
 617 from the droplet in Roy et al., (2023). The evaporating droplet temperature essentially keeps adjusting to the
 618 thermodynamic wet-bulb temperature of its immediate changing environment. Therefore, the more realistic
 619 simulations of evaporating cloud droplets that include the effect of spatiotemporally varying ambient air thermal and
 620 vapor density gradients, as shown in this study, reveal that droplets can potentially achieve even lower temperatures
 621 than previously known or estimated from past studies (Srivastava and Coen, 1992; Roy et al., 2023). The decrease in
 622 droplet temperatures from their initial temperatures can be much larger, especially for drier environments, as much as
 623 25.8 K for $RH_\infty = 10\%$ and 5.0 K for $RH_\infty = 70\%$, for an environment with $P = 500$ hPa, and $T_\infty = 273.15$ K (Table 1
 624 and Fig. 15a). As shown in Fig. 15, the magnitude of reduction in droplet temperatures decreases with higher ambient
 625 RH_∞ and P , and lower T_∞ , similar to previous studies (Srivastava and Coen, 1992; Roy et al., 2023).



626
 627 **Figure 16: Comparison between droplet lifetimes (as defined in this study) calculated using the classical diffusion-limited**
 628 **evaporation approach (solid lines), bulk droplet model from Roy et al., (2023) (dashed lines), and this study (dashed-dotted**
 629 **lines), for initial droplet radii, $r_0 = 30 \mu\text{m}$ (upper panel), and $50 \mu\text{m}$ (lower panel), relative humidities ($RH_\infty = 10, 40, 70\%$),**
 630 **and pressures, $P = 500$ hPa (left column), and 850 hPa right column), and ambient temperature, $T_\infty = 273.15$ K (0°C , red),**
 631 **268.15 K (-5°C , green) and 263.15 K (-10°C , blue). $10 \mu\text{m}$ droplets (not shown here) have much smaller lifetimes compared**
 632 **to 30 and $50 \mu\text{m}$ droplets.**



633 Table 2 and Fig. 16 provide comparisons between 30 and 50 μm droplet lifetimes (as defined earlier in Sec. 3a) using
634 the classical pure-diffusion-limited evaporation approach (t_{LC}), which ignores evaporative cooling at the droplet
635 surface (Maxwell, 1890; Eq 13-10 of Pruppacher and Klett, 1997), the “bulk” droplet approach as described in Roy et
636 al., (2023) (t_{RRD}), which ignores internal droplet heat transfer and spatiotemporally varying thermal and moisture
637 gradients in the ambient air, and results from this study (t_L). The magnitude of t_L is greater than the corresponding
638 values of t_{LC} and t_{RRD} . This is because the droplet temperatures in this study never reach steady-state and are much
639 lower than the corresponding droplet temperatures from the diffusion-limited approach ($\sim T_\infty$), and Roy et al., (2023)
640 ($\sim T_{RRD}$). This can be explained by the greater decrease in evaporating droplet temperature leading to a greater reduction
641 in saturation vapor pressure at the droplet surface. This results in a slower droplet evaporation rate, therefore increasing
642 the droplet lifetime. As shown in Fig. 16, this increase in droplet lifetime depends on the environmental subsaturation,
643 ambient temperatures, and pressures, with a greater increase for more humid, higher pressure, and lower ambient
644 temperature environments. This increase in droplet lifetimes can potentially enhance ice nucleation by increasing the
645 chances of activation of ice nucleating particles (INPs) within the supercooled cloud droplets (see Section 5b).

646

647 **5.2 Implications for ice nucleation**

648

649 Ice nucleation rates are influenced by temperature (Wright and Petters, 2013; Kanji et al., 2017) and time (Vali, 1994).
650 There are two theories in ice nucleation modeling: the time-independent “singular hypothesis,” which suggests
651 instantaneous ice formation, and the time-dependent “stochastic hypothesis,” which proposes that ice clusters in
652 embryos form and vanish continually, with a frequency that depends on temperature. Supercooled cloud droplet
653 temperatures and their lifetimes are potential contributing factors for the enhancement of ice formation within
654 evaporating regions of clouds such as cloud-tops and edges. As discussed in Roy et al., (2023), evaporative cooling
655 of supercooled cloud droplets in subsaturated environments can enhance ice nucleation near cloud boundaries in two
656 ways: by instantly increasing ice-nucleating particle activation due to lower droplet temperatures (consistent with the
657 singular hypothesis) and/or by extending supercooled droplet lifetimes, allowing more time for nucleation events
658 (consistent with the stochastic hypothesis). Based on limited laboratory investigations available on time dependency
659 of heterogeneous ice nucleation, conducted between temperatures -14 and -30 $^\circ\text{C}$, varying fractions of the droplets
660 were reported to freeze within a range of 1 s to 500 s (Welti et al., 2012; Broadley et al., 2012; Murray et al., 2012;
661 Jakobsson et al., 2022). As shown in Table 2 and Fig. 16, droplet lifetimes as estimated from both approaches (t_{RRD}
662 and t_L), which include droplet evaporative cooling, are longer as compared to the classical diffusion-limited
663 evaporation approach (t_{LC}), allowing more time for potential occurrence of an ice nucleation event. For temperatures
664 between -5 $^\circ\text{C}$ and -10 $^\circ\text{C}$, for the three different subsaturated environments ($RH_\infty = 10, 40, \text{ and } 70\%$) examined in
665 this analysis, t_{RRD} typically ranged from 0.7-4.2 s for 10 μm , 6-38 s for 30 μm and 18-105 s for 50 μm initial radius
666 of droplets, respectively. For similar environments, $t_L > t_{RRD} > t_C$, with t_L typically ranging from 1.1-5.7 s for 10 μm ,
667 11-61 s for 30 μm and 33-176 s for 50 μm initial radii droplets, respectively. For larger droplets, say 30 and 50 μm ,
668 the droplets survive much longer as compared to 10 μm droplets, likely enhancing the chances of an ice nucleation
669 event. Comparing these values with reported droplet freezing timescales available from experimental studies, droplet



670 freezing events can potentially occur within the time frame when these droplets can reach lower temperatures due to
671 evaporative cooling before they completely dissipate into the subsaturated air. Results from this study further
672 strengthen evidence of the hypothesized mechanism of enhancement of ice nucleation via droplet evaporation.
673 Together with the consistent observation of supercooled water in cloud-top generating cells (Plummer et al., 2014;
674 Zaremba et al., 2024), these results contribute to explaining the observations of the prodigious production of ice
675 particles produced in generating cells at the cloud-tops of winter storms (e.g., Plummer et al., 2015).

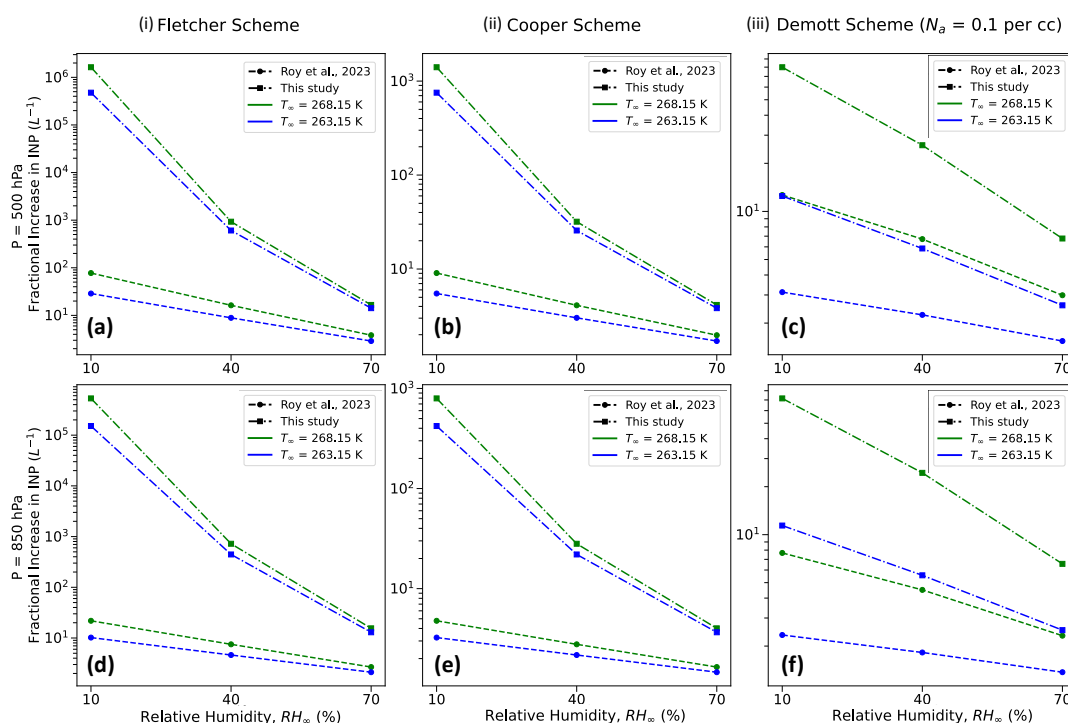
676
677 Due to the observational evidence of a higher dependency of ice nucleation on temperature than time (Wright and
678 Petters, 2013), and the increased difficulty of representing time-dependent stochastic nucleation in numerical models,
679 the simpler and more widely used approach is to use the time-dependent singular hypothesis framework to simulate
680 ice initiation processes. Drawing from theoretical insights, laboratory experiments, and field campaigns, numerous
681 parameterization methods for modeling heterogeneous ice nucleation in cloud and climate models have been created
682 over the years (Fletcher, 1962; Cooper, 1986; Meyers et al., 1992; DeMott et al., 1998; Khvorostyanov and Curry,
683 2000; Phillips et al., 2008). Most of the conventionally used schemes (Fletcher, 1962; Cooper, 1986; Demott et al.,
684 2010) share a common feature, which is the utilization of the ambient air temperature for estimating activated INPs,
685 as opposed to relying on the droplet temperature, even for primary ice-nucleation modes such as immersion freezing
686 and contact nucleation.

687
688 Similar to Roy et al. (2023), we investigate the maximum enhancement in activated INP concentrations that can occur
689 due to evaporative cooling of supercooled water droplets in a spatiotemporally varying environment, assuming that
690 the activation in the parameterization schemes (Fletcher, 1962; Cooper, 1986; Demott et al., 2010) is related to the
691 droplet temperatures towards the end of their lifetimes (T_L) rather than the ambient temperature. Fig. 17 presents a
692 comparison between Roy et al. (2023), and the current study in terms of the highest fractional increase in activated
693 ice-nucleating particles (INPs), as projected through the Fletcher, Cooper, and Demott schemes (considering ambient
694 aerosol concentration, N_a , with diameters greater than $0.5 \mu\text{m}$). Owing to even lower droplet temperatures during
695 evaporation, the fractional increase in activated INPs is higher as calculated from this study, with several orders of
696 magnitude increase for drier environments. For example, the Fletcher Scheme predicts an enhancement in activated
697 INPs by a factor of $\sim 10^6$ for $RH_\infty = 10\%$, $T_\infty = 268.15 \text{ K}$, $P = 500 \text{ hPa}$ based on droplet temperatures from this study,
698 while the corresponding number from Roy et al. (2023) is ~ 100 (Fig. 17a). The fractional increases are slightly smaller
699 for higher pressure environments due to lower evaporative cooling of the droplets under such conditions (compare
700 Figs. 17a, d, b,e, and c,f). Consistent with previous results from Roy et al. (2023), compared to the Fletcher Scheme,
701 the Cooper and Demott schemes demonstrate relatively lower enhancement in activated INPs. For the same
702 environment stated earlier, the corresponding activated INP enhancement factor values for Cooper and Demott
703 schemes are $\sim 10^3$ and 80, respectively (Figs. 17b and c).

704
705 Therefore, results from the current study further corroborate the hypothesized ice nucleation enhancement mechanism
706 through evaporative cooling of supercooled droplets (Mossop et al., 1968; Young, 1974; Beard, 1992; Roy et al.,



707 2023), providing much higher estimates of activated INP concentrations from previous analyses (Roy et al., 2023).
 708 This potential increase in INP concentrations in subsaturated environments near cloud tops and edges, particularly at
 709 higher sub-freezing temperatures, may partially help resolve the several orders of magnitude discrepancy between
 710 predicted INP and observed ice particle concentrations in such regions of the cloud. To evaluate the effectiveness of
 711 the potential ice-nucleation enhancement mechanism through evaporation, future modeling experiments within a
 712 robust dynamical model setup, considering a population of both freezing and evaporating droplets, along with their
 713 lifetimes, droplet-droplet interaction, different species of INPs, impact of turbulence and other feedbacks, are required.
 714



715
 716 **Figure 17: Comparison between the maximum fractional increase in INPs as estimated by Roy et al., (2023) and this study**
 717 **for three different parameterization schemes: (i) Fletcher (1962) (ii) Cooper (1986), and (iii) Demott et al., (2010), for three**
 718 **different environmental relative humidities ($RH_{\infty} = 10, 40$ and 70%), and two ambient temperatures ($T_{\infty} = 268.15$ K (-5° C)**
 719 **and 263.15 K (-10° C)) and two different pressures ($P = 500$ and 850 hPa).**

720

721 6 Conclusions

722

723 In this study, we presented a quantitative investigation the temperature and lifetime of an evaporating droplet,
 724 considering internal thermal gradients within the droplet as well as resolving thermal and vapor density gradients in
 725 the surrounding ambient air. The computational approach involved solving the Navier-Stokes and continuity
 726 equations, coupled with heat and vapor diffusion equations, using an advanced numerical model that employs the
 727 finite element method. This is the first simulation of the spatiotemporal evolution of droplet temperature, radius, and



728 its environment for an isolated, stationary, and supercooled cloud droplet evaporating in various subsaturated
729 environmental conditions. Various ambient pressure (P), temperature (T_∞), relative humidity (RH_∞), and initial droplet
730 radii (r_0) were considered. The motivation behind this study was to provide more exacting calculations to support the
731 hypothesized ice nucleation enhancement mechanism due to the evaporation of supercooled cloud droplets at cloud
732 boundaries, such as cloud-top ice-generating cells, and for ambient temperatures between 0°C and -10°C where ice
733 nucleation is least effective.

734
735 Since evaporation is a surface phenomenon, there is a legitimate interest in computing droplet internal thermal
736 gradients and investigating if the droplet surface gets preferentially cooled during droplet evaporation, with regards to
737 the activation of ice nucleating particles. The numerical simulations show for typical cloud droplet sizes ($r_0 = 10, 30,$
738 $50\ \mu\text{m}$) and environmental conditions considered here, the internal thermal gradients dissipate quite quickly ($\leq 0.3\ \text{s}$)
739 when the droplet is introduced to a new subsaturated environment. Thus, spatial thermal gradients within the droplet
740 can be reasonably ignored. Hence, one can potentially ignore the extra computational expense of simulating
741 conductive heat transfer within the droplet for timescales $> 1\ \text{s}$.

742
743 The results from this study support findings from the literature that an evaporating supercooled cloud droplet can exist
744 at a temperature lower than that of the ambient atmosphere and corroborate the tendencies of the dependence of
745 decrease in droplet temperatures on environmental factors and initial droplet sizes (Srivastava and Coen, 1992; Roy
746 et. al, 2023). Decreases in droplet temperatures are smaller for higher ambient RH_∞ and P , and lower T_∞ , qualitatively
747 in accordance with previous studies (Srivastava and Coen, 1992; Roy et al., 2023). The novelty of this study lies in
748 demonstrating that the magnitude of droplet cooling can be much higher than estimated from past studies of droplet
749 evaporation, especially for drier environments. For a droplet evaporating in an environment with $P = 500\ \text{hPa}$, $T_\infty =$
750 $268.15\ \text{K}$ (-5°C), $RH_\infty = 10\%$, Roy et al., (2023) estimated a $7.3\ \text{K}$ decrease in droplet temperature, while this study
751 shows that there can be as much as a $23.8\ \text{K}$ decrease in droplet temperature. This is because previous studies assumed
752 prescribed ambient environments at all distances from the droplet, while this analysis shows that as a droplet
753 evaporates and cools, the air in the vicinity of the droplet cools as well, giving rise to spatiotemporally varying thermal
754 and vapor density fields in the immediate environment surrounding the droplet. Here, the net conductive warming
755 from the environmental air enveloping the droplet is lower as compared to Roy et al., (2023), effectively leading to a
756 much lower droplet temperature. At a particular time, the strength and radial dependence of these gradients depend on
757 the subsaturation of the air medium and the magnitude of droplet cooling due to evaporation, with the largest cooling
758 at lower RH_∞ . In this study, the temperature and vapor density in the ambient air continually evolve, thus affecting the
759 transfer of heat and vapor between the droplet surface and the environment far away from the droplet. This affects the
760 temperature evolution and decay rates of the evaporating droplet to a greater degree than shown in previous studies
761 for a similar environment (Srivastava and Cohen, 1992; Roy et al. 2023).

762
763 This study also demonstrated that the lifetimes of the evaporating droplets are longer compared to Roy et al. (2023)
764 because as the droplet temperature gets lower, the saturation vapor pressure at the droplet surface reduces, leading to



765 a weaker evaporation rate. For an environment with $P = 500$ hPa, $T_{\infty} = 268.15$ K (-5°C), $RH_{\infty} = 10\%$, a $50\ \mu\text{m}$ droplet
766 reaches the end of its lifetime, as defined in this study, in 32.8s, while the corresponding values for the diffusion-
767 limited evaporation approach as estimated from Roy et. al, (2023) are 9.6 s and 17.9 s, respectively. The rates of
768 evaporation tend to be lower in this study due to even lower droplet temperatures as well as spatiotemporally varying
769 vapor density gradients around the droplets. As the droplet evaporates, the envelope of air surrounding the droplet is
770 colder, has lower values of diffusivity leading to lower evaporation rates, and has higher vapor concentration than the
771 ambient air, thus decreasing the evaporation rates.

772

773 To summarize, if one considers the more realistic case of droplet evaporation, including the spatiotemporally varying
774 thermal and vapor density gradients in the vicinity of the water droplet, the evaporating droplet can experience a
775 substantial reduction in temperatures by tens of degrees, strongly dependent on the ambient relative humidity and
776 weakly dependent on ambient pressure and temperature. Similar to the case of an isolated, stationary droplet
777 evaporating in a prescribed ambient environment, the droplet almost immediately reaches its inflection point
778 temperature, which can be well-approximated by the thermodynamic wet-bulb temperature of the initial ambient
779 environment around the droplet. However, unlike the former case, the droplet temperatures in this study continue to
780 steadily decrease as they adjust to the evolving thermodynamic wet-bulb temperature of the surrounding air. In more
781 humid environments, the droplets may not experience a larger droplet cooling, but their lifetimes, as defined in this
782 study, get extended by tens of seconds as compared to the classical estimation which neglects droplet cooling.

783

784 The current analysis also demonstrates that lower evaporating droplet temperatures would lead to an enhancement of
785 activated INPs from three widely used INP parameterization schemes, further corroborating the hypothesized ice
786 nucleation enhancement mechanism through evaporative cooling of supercooled droplets. Notably, the estimates of
787 activated INP concentrations from this study are higher than previous analyses, as the droplet temperatures are much
788 lower towards the end of their lifetimes, with several orders of magnitude increase in activated INPs for drier
789 environments. The Fletcher Scheme predicts the greatest enhancement in activated INPs by a factor of $\sim 10^6$ for RH_{∞}
790 $= 10\%$, $T_{\infty} = 268.15$ K, $P = 500$ hPa, while the corresponding enhancement factor values for Cooper and Demott
791 schemes are $\sim 10^3$ and 80, respectively.

792

793 This study suggests a need for a more in-depth examination of supercooled cloud droplet temperatures and their
794 lifetimes in subsaturated environments, especially when simulating heterogeneous ice nucleation processes that
795 require the presence of supercooled water droplets. This is crucial because the concentration of activated ice-
796 nucleating particles (INPs) is influenced by both droplet temperature and how long evaporating droplets persist.
797 Additionally, the findings from this investigation may also partially help understand disparities between observed ice
798 particle concentrations and activated INPs, especially at relatively higher sub- 0°C temperatures. Including the effect
799 of droplet evaporative cooling on droplet temperatures and lifetimes, while modeling cloud microphysical processes
800 in subsaturated environments, will also lead to improved accuracy of the evolution of the droplet size distribution as
801 well as primary ice nucleation mechanisms.



802 **Author contribution:** PR, RMR and LDG conceptualized the problem and numerical experiments. PR designed and
803 performed the simulations, analyzed the data, and prepared the first draft of the manuscript. RMR and LDG reviewed
804 and edited the manuscript. RMR and LDG acquired required funding for the project.

805

806 **Competing interests:** The authors have no competing interests.

807

808 **Acknowledgements:** This work was funded by the NASA CAMP²Ex program under grant 80NSSC18K0144 and the
809 NASA Earth Venture Suborbital-3 (EVS-3) IMPACTS program under grant 80NSSC19K0355. This research was
810 also supported by the National Science Foundation under grant NSF AGS-2016106.

811

812 **Code/Data availability:** This modeling analysis used the proprietary COMSOL Multiphysics version 6.0 software
813 package which can be licensed through <https://www.comsol.com/>.

814

815 **References**

816

817 Alduchov, O.A. and Eskridge, R.E.: Improved Magnus form approximation of saturation vapor pressure, *Journal of*
818 *Applied Meteorology and Climatology*, 35(4), pp.601-609, [https://doi.org/10.1175/1520-](https://doi.org/10.1175/1520-0450(1996)035<0601:IMFAOS>2.0.CO;2)
819 [0450\(1996\)035<0601:IMFAOS>2.0.CO;2](https://doi.org/10.1175/1520-0450(1996)035<0601:IMFAOS>2.0.CO;2), 1996.

820 Beard, K.: Ice Initiation in warm-base convective clouds: An assessment of microphysical mechanisms, *Atmos. Res.*,
821 28, 125-152, [https://doi.org/10.1016/0169-8095\(92\)90024-5](https://doi.org/10.1016/0169-8095(92)90024-5), 1992.

822 Broadley, S.L., Murray, B.J., Herbert, R.J., Atkinson, J.D., Dobbie, S., Malkin, T.L., Condcliffe, E. and Neve, L.:
823 Immersion mode heterogeneous ice nucleation by an illite rich powder representative of atmospheric mineral
824 dust, *Atmospheric Chemistry and Physics*, 12(1), pp.287-307, <https://doi.org/10.5194/acp-12-287-2012>,
825 2012.

826 Chushak, Y.G. and Bartell, L.S.: Simulations of spontaneous phase transitions in large, deeply supercooled clusters
827 of SeF₆, *The Journal of Physical Chemistry B*, 103(50), pp.11196-11204, <https://doi.org/10.1021/jp992818g>,
828 1999.

829 Chushak, Y. and Bartell, L.S.: Crystal nucleation and growth in large clusters of SeF₆ from molecular dynamics
830 simulations, *The Journal of Physical Chemistry A*, 104(41), pp.9328-9336,
831 <https://doi.org/10.1021/jp002107e>, 2000.

832 COMSOL 2023a Cylindrical System Documentation, Last Accessed Sept 15, 2023

833 https://doc.comsol.com/5.5/doc/com.comsol.help.comsol/comsol_ref_definitions.12.090.html

834 COMSOL 2023b Infinite Element Domain Documentation, Last Accessed Sept 15, 2023

835 https://doc.comsol.com/5.5/doc/com.comsol.help.comsol/comsol_ref_definitions.12.116.html

836 COMSOL 2023c Free Triangular Documentation, Last Accessed Sept 15, 2023

837 https://doc.comsol.com/5.5/doc/com.comsol.help.comsol/comsol_ref_mesh.15.38.html

838 COMSOL 2023d Mapped Documentation, Last Accessed Sept 15, 2023

839 https://doc.comsol.com/5.6/doc/com.comsol.help.comsol/comsol_ref_mesh.20.40.html



- 840 Cooper, W.A.: Ice initiation in natural clouds. In *Precipitation enhancement—A scientific challenge* (pp. 29-32).
841 American Meteorological Society, Boston, MA, <https://doi.org/10.1175/0065-9401-21.43.29>, 1986.
- 842 DeMott, P.J., Rogers, D.C., Kreidenweis, S.M., Chen, Y., Twohy, C.H., Baumgardner, D., Heymsfield, A.J. and Chan,
843 K.R.: The role of heterogeneous freezing nucleation in upper tropospheric clouds: Inferences from
844 SUCCESS, *Geophysical Research Letters*, 25(9), pp.1387-1390, <https://doi.org/10.1029/97GL03779>, 1998.
- 845 DeMott, P.J., Prenni, A.J., Liu, X., Kreidenweis, S.M., Petters, M.D., Twohy, C.H., Richardson, M.S., Eidhammer,
846 T. and Rogers, D.: Predicting global atmospheric ice nuclei distributions and their impacts on
847 climate, *Proceedings of the National Academy of Sciences*, 107(25), pp.11217-11222,
848 <https://doi.org/10.1073/pnas.0910818107>, 2010.
- 849 Djikaev, Y.S., Tabazadeh, A., Hamill, P. and Reiss, H.: Thermodynamic conditions for the surface-stimulated
850 crystallization of atmospheric droplets, *The Journal of Physical Chemistry A*, 106(43), pp.10247-10253,
851 <https://doi.org/10.1021/jp021044s>, 2002.
- 852 Djikaev, Y.S. and Ruckenstein, E.: Thermodynamics of heterogeneous crystal nucleation in contact and immersion
853 modes, *The Journal of Physical Chemistry A*, 112(46), pp.11677-11687, <https://doi.org/10.1021/jp803155f>,
854 2008.
- 855 Fletcher, N.H.: *The physics of rainclouds/NH Fletcher; with an introductory chapter by P. Squires and a foreword by*
856 *EG Bowen*. Cambridge University Press, <https://doi.org/10.1002/qj.49708837821>, 1962.
- 857 Fukuta, N.: Theories of competitive cloud droplet growth and their application to cloud physics studies, *Journal of*
858 *the Atmospheric Sciences*, 49, 1107–1114, [https://doi.org/10.1175/1520-](https://doi.org/10.1175/1520-0469(1992)049<1107:TOCCDG>2.0.CO;2)
859 [0469\(1992\)049<1107:TOCCDG>2.0.CO;2](https://doi.org/10.1175/1520-0469(1992)049<1107:TOCCDG>2.0.CO;2), 1992.
- 860 Grabowski, W.W. and Wang, L.P.: Growth of cloud droplets in a turbulent environment, *Annual Review of Fluid*
861 *Mechanics*, 45, pp.293-324, <https://doi.org/10.1146/annurev-fluid-011212-140750>, 2013.
- 862 Hall, W.D. and Pruppacher, H.R.: The survival of ice particles falling from cirrus clouds in subsaturated air, *Journal*
863 *of Atmospheric Sciences*, 33(10), pp.1995-2006, [https://doi.org/10.1175/1520-](https://doi.org/10.1175/1520-0469(1976)033<1995:TSOIPF>2.0.CO;2)
864 [0469\(1976\)033<1995:TSOIPF>2.0.CO;2](https://doi.org/10.1175/1520-0469(1976)033<1995:TSOIPF>2.0.CO;2), 1976.
- 865 Jakobsson, J.K., Waman, D.B., Phillips, V.T. and Bjerring Kristensen, T.: Time dependence of heterogeneous ice
866 nucleation by ambient aerosols: laboratory observations and a formulation for models. *Atmospheric*
867 *Chemistry and Physics*, 22(10), pp.6717-6748, <https://doi.org/10.5194/acp-22-6717-2022>, 2022.
- 868 Kanji, Z. A., Ladino, L. A., Wex H., Boose, Y., Burkert-Kohn, M., Cziczo, D. J. and Krämer, M.: Overview of Ice
869 Nucleating Particles, *Meteor. Monogr.*, **58**, 1.1–1.33, [https://doi.org/10.1175/AMSMONOGRAPHS-D-16-](https://doi.org/10.1175/AMSMONOGRAPHS-D-16-0006.1)
870 [0006.1](https://doi.org/10.1175/AMSMONOGRAPHS-D-16-0006.1), 2017.
- 871 Khain, A.P. and Pinsky, M.: *Physical processes in clouds and cloud modeling*, Cambridge University Press, 2018.
- 872 Khvorostyanov, V.I. and Curry, J.A.: A new theory of heterogeneous ice nucleation for application in cloud and
873 climate models, *Geophysical Research Letters*, 27(24), pp.4081-4084,
874 <https://doi.org/10.1029/1999GL011211>, 2000.



- 875 Khvorostyanov, V. and Sassen, K.: Toward the theory of homogeneous nucleation and its parameterization for cloud
876 models, *Geophysical research letters*, 25(16), pp.3155-3158, <https://doi.org/10.1029/98GL02332>, 1998.
- 877 Kinzer, G. D., and Gunn, R.: The evaporation, temperature and thermal relaxation-time of freely falling waterdrops,
878 *J. Meteor.*, 8, 71–83. [https://doi.org/10.1175/1520-0469\(1951\)008<0071:TETATR>2.0.CO;2](https://doi.org/10.1175/1520-0469(1951)008<0071:TETATR>2.0.CO;2), 1951.
- 879 Lü, Y.J., Xie, W.J. and Wei, B.: Observation of ice nucleation in acoustically levitated water drops, *Applied Physics*
880 *Letters*, 87(18), <http://dx.doi.org/10.1063/1.2126801>, 2005.
- 881 Marquis, J. and Harrington, J.Y.: Radiative influences on drop and cloud condensation nuclei equilibrium in
882 stratocumulus, *Journal of Geophysical Research: Atmospheres*, 110(D10),
883 <https://doi.org/10.1029/2004JD005401>, 2005.
- 884 Maxwell, J.C.: Theory of the wet bulb thermometer, *Scientific Papers of James Clerk Maxwell*, 2, p.636, 1890.
- 885 Meyers, M.P., DeMott, P.J. and Cotton, W.R.: New primary ice-nucleation parameterizations in an explicit cloud
886 model, *Journal of Applied Meteorology and Climatology*, 31(7), pp.708-721, [https://doi.org/10.1175/1520-0450\(1992\)031<0708:NPINPI>2.0.CO;2](https://doi.org/10.1175/1520-0450(1992)031<0708:NPINPI>2.0.CO;2), 1992.
- 888 Mossop, S.C., Ruskin, R.E. and Heffernan, K.J.: Glaciation of a Cumulus at Approximately– 4C, *Journal of*
889 *Atmospheric Sciences*, 25(5), pp.889-899, [https://doi.org/10.1175/1520-0469\(1968\)025<0889:GOACAA>2.0.CO;2](https://doi.org/10.1175/1520-0469(1968)025<0889:GOACAA>2.0.CO;2), 1968.
- 891 Murray, B.J., O'sullivan, D., Atkinson, J.D. and Webb, M.E.: Ice nucleation by particles immersed in supercooled
892 cloud droplets, *Chemical Society Reviews*, 41(19), pp.6519-6554, doi:10.1039/c2cs35200a., 2012.
- 893 Phillips, V.T., DeMott, P.J. and Andronache, C.: An empirical parameterization of heterogeneous ice nucleation for
894 multiple chemical species of aerosol, *Journal of the Atmospheric Sciences*, 65(9), pp.2757-2783,
895 <https://doi.org/10.1175/2007JAS2546.1>, 2008.
- 896 Plummer, D.M., McFarquhar, G.M., Rauber, R.M., Jewett, B.F. and Leon, D.C.: Structure and statistical analysis of
897 the microphysical properties of generating cells in the comma head region of continental winter cyclones,
898 *Journal of the Atmospheric Sciences*, 71(11), pp.4181-4203, <https://doi.org/10.1175/JAS-D-14-0100.1>, 2014.
- 899 Plummer, D. M., G. M. McFarquhar, R. M. Rauber, B. F. Jewett, and Leon., D. C.: Microphysical properties of
900 convectively generated fall streaks in the comma head region of continental winter cyclones, *J. Atmos.*
901 *Sci.*, 72, 2465–2483, doi:10.1175/JAS-D-14-0354.1, 2015.
- 902 Pruppacher, H. R., and Klett, J. D.: *Microphysics of Clouds and Precipitation*. 2d ed. Kluwer Academic, 954 pp.,
903 1997.
- 904 Ramelli, F., Henneberger, J., David, R.O., Bühl, J., Radenz, M., Seifert, P., Wieder, J., Lauber, A., Pasquier, J.T.,
905 Engelmann, R. and Mignani, C.: Microphysical investigation of the seeder and feeder region of an Alpine
906 mixed-phase cloud, *Atmospheric Chemistry and Physics*, 21(9), pp.6681-6706, <https://doi.org/10.5194/acp-21-6681-2021>, 2021.
- 908 Roach, W. T.: On the effect of radiative exchange on the growth by condensation of a cloud or fog droplet, *Quart. J.*
909 *Roy. Meteor. Soc.*, 102, 361–372, <https://doi.org/10.1002/qj.49710243207>, 1976.
- 910 Rogers, R.R. and Yau, M.K.: *A Short Course in Cloud Physics*. Pergamon Press, 294 pp., 1989.



- 911 Rowe, P.M., Fergoda, M. and Neshyba, S.: Temperature-dependent optical properties of liquid water from 240 to 298
912 K. *Journal of Geophysical Research: Atmospheres*, 125(17), <https://doi.org/10.1029/2020JD032624>, 2020.
- 913 Roy, P., Rauber, R.M. and Girolamo, L.D.: A closer look at the evolution of supercooled cloud droplet temperature
914 and lifetime in different environmental conditions with implications for ice nucleation in the evaporating
915 regions of clouds, *Journal of the Atmospheric Sciences*. <https://doi.org/10.1175/JAS-D-22-0239.1>, 2023.
- 916 Satoh, I., Fushinobu, K. and Hashimoto, Y.: Freezing of a water droplet due to evaporation—heat transfer dominating
917 the evaporation–freezing phenomena and the effect of boiling on freezing characteristics, *International*
918 *Journal of Refrigeration*, 25(2), pp.226-234, [http://dx.doi.org/10.1016/S0140-7007\(01\)00083-4](http://dx.doi.org/10.1016/S0140-7007(01)00083-4), 2002.
- 919 Scardovelli, R. and Zaleski, S.: Direct numerical simulation of free-surface and interfacial flow, *Annual review of fluid*
920 *mechanics*, 31(1), pp.567-603. <https://doi.org/10.1146/annurev.fluid.31.1.567>, 1999.
- 921 Sedunov, Y. S.: *Physics of the Drop Formation in the Atmosphere*, John Wiley and Sons, 234 pp., 1974.
- 922 Shaw, R.A., Durant, A.J. and Mi, Y.: Heterogeneous surface crystallization observed in undercooled water, *The*
923 *Journal of Physical Chemistry B*, 109(20), pp.9865-9868, <https://doi.org/10.1021/jp0506336>, 2005.
- 924 Srivastava, R.C. and Coen, J.L.: New explicit equations for the accurate calculation of the growth and evaporation of
925 hydrometeors by the diffusion of water vapor, *Journal of Atmospheric Sciences*, 49(17), pp.1643-1651,
926 [https://doi.org/10.1175/1520-0469\(1992\)049<1643:NEEFTA>2.0.CO;2](https://doi.org/10.1175/1520-0469(1992)049<1643:NEEFTA>2.0.CO;2), 1992.
- 927 Standard Atmosphere: ISO 2533:1975, updated 2021: <https://www.iso.org/standard/7472.html>, 2021, last accessed
928 09/26/2022.
- 929 Szakáll, M., Debertshäuser, M., Lackner, C.P., Mayer, A., Eppers, O., Diehl, K., Theis, A., Mitra, S.K. and Borrmann,
930 S.: Comparative study on immersion freezing utilizing single-droplet levitation methods, *Atmospheric*
931 *Chemistry and Physics*, 21(5), pp.3289-3316, <https://doi.org/10.5194/acp-21-3289-2021>, 2021.
- 932 Tabazadeh, A., Djikaev, Y.S., Hamill, P. and Reiss, H.: Laboratory evidence for surface nucleation of solid polar
933 stratospheric cloud particles, *The Journal of Physical Chemistry A*, 106(43), pp.10238-10246,
934 <https://doi.org/10.1021/jp021045k>, 2002a.
- 935 Tabazadeh, A., Djikaev, Y.S. and Reiss, H.: Surface crystallization of supercooled water in clouds, *Proceedings of*
936 *the National Academy of Sciences*, 99(25), pp.15873-15878, <https://doi.org/10.1073/pnas.252640699>, 2002b.
- 937 Tessendorf, S.A., Boe, B., Geerts, B., Manton, M.J., Parkinson, S. and Rasmussen, R.: The future of winter orographic
938 cloud seeding: A view from scientists and stakeholders, *Bulletin of the American Meteorological Society*,
939 96(12), pp.2195-2198, <https://doi.org/10.1175/BAMS-D-15-00146.1>, 2015.
- 940 Vaillancourt, P.A., Yau, M.K. and Grabowski, W.W.: Microscopic approach to cloud droplet growth by condensation.
941 Part I: Model description and results without turbulence, *Journal of the Atmospheric Sciences*, 58(14),
942 pp.1945-1964, [https://doi.org/10.1175/1520-0469\(2001\)058%3C1945:MATCDG%3E2.0.CO;2](https://doi.org/10.1175/1520-0469(2001)058%3C1945:MATCDG%3E2.0.CO;2), 2001.
- 943 Vali, G.: Freezing Rate Due to Heterogeneous Nucleation. *J. Atmos. Sci.*, **51**, 1843–
944 1856, [https://doi.org/10.1175/1520-0469\(1994\)051<1843:FRDTHN>2.0.CO;2](https://doi.org/10.1175/1520-0469(1994)051<1843:FRDTHN>2.0.CO;2), 1994.
- 945 Volmer, M.: *Kinetic der Phasenbildung* (Steinkopff, Dresden, Leipzig), 1939.
- 946 Wang, Y., McFarquhar, G.M., Rauber, R.M., Zhao, C., Wu, W., Finlon, J.A., Stechman, D.M., Stith, J., Jensen, J.B.,
947 Schnaiter, M. and Järvinen, E.: Microphysical properties of generating cells over the Southern Ocean: Results



948 from SOCRATES, *Journal of Geophysical Research: Atmospheres*, 125(13),
949 <https://doi.org/10.1029/2019JD032237>, 2020.

950 Watts, R.G.: Relaxation time and steady evaporation rate of freely falling raindrops, *Journal of Atmospheric Sciences*,
951 28(2), pp.219-225, [https://doi.org/10.1175/1520-0469\(1971\)028<0219:RTASER>2.0.CO;2](https://doi.org/10.1175/1520-0469(1971)028<0219:RTASER>2.0.CO;2), 1971.

952 Watts, R.G. and Farhi, I.: Relaxation times for stationary evaporating liquid droplets, *Journal of the Atmospheric*
953 *Sciences*, 32(9), pp.1864-1867, [https://doi.org/10.1175/1520-0469\(1975\)032%3C1864:RTFSEL%3E2.0.CO;2](https://doi.org/10.1175/1520-0469(1975)032%3C1864:RTFSEL%3E2.0.CO;2), 1975.

954
955 Welti, A., Lüönd, F., Kanji, Z.A., Stetzer, O. and Lohmann, U.: Time dependence of immersion freezing: an
956 experimental study on size selected kaolinite particles. *Atmospheric Chemistry and Physics*, 12(20), pp.9893-
957 9907, 2012.

958 Wexler, A.: Vapor pressure formulation for water in range 0 to 1008C. A revision, *J. Res. Natl. Bur. Stand. (U.S.)*,
959 80A, 775–785, <https://doi.org/10.6028%2Fjres.080A.071>, 1976.

960 Wright, T. P., and Petters, M.D.: The role of time in heterogeneous freezing nucleation, *J. Geophys. Res.*, 118, 3731–
961 3743, <https://doi.org/10.1002/jgrd.50365>, 2013.

962 Yang, K., Hong, F. and Cheng, P.: A fully coupled numerical simulation of sessile droplet evaporation using Arbitrary
963 Lagrangian–Eulerian formulation. *International Journal of Heat and Mass Transfer*, 70, pp.409-420,
964 <https://doi.org/10.1016/j.ijheatmasstransfer.2013.11.017>, 2014.

965 Young, K. C.: The Role of Contact Nucleation in Ice Phase Initiation in Clouds, *Journal of the Atmospheric Sciences*,
966 31, 768–776,
967 [https://doi.org/10.1175/1520-0469\(1974\)031<0768:TROCNI>2.0.CO;2](https://doi.org/10.1175/1520-0469(1974)031<0768:TROCNI>2.0.CO;2), 1974.

968 Zaremba, T.J., Rauber, R.M., Heimes, K., Yorks, J.E., Finlon, J.A., Nicholls, S.D., Selmer, P., McMurdie, L.A. and
969 McFarquhar, G.M.: Cloud-Top Phase Characterization of Extratropical Cyclones over the Northeast and
970 Midwest United States: Results from IMPACTS, *Journal of the Atmospheric Sciences*, 81(2), pp.341-361,
971 <https://doi.org/10.1175/JAMC-D-22-0154.1>, 2024.

972
973